Winter 2010

Design of an Integrated Starter-Alternator for a Series Hybrid Electric Vehicle: A Case Study in Axial Flux Permanent Magnet Machine Design

Jessica L. Colton
University of Nebraska at Lincoln, colton.jessica@huskers.unl.edu

Design of an Integrated Starter-Alternator for a Series Hybrid Electric Vehicle:

A Case Study in Axial Flux Permanent Magnet Machine Design

by

Jessica Colton

A DISSERTATION

Presented to the Faculty of

The Graduate College at the University of Nebraska

In Partial Fulfillment of Requirements

For the Degree of Doctor of Philosophy

Major: Interdepartmental Area of Engineering
(Electrical Engineering)

Under the Supervision of Professors Jerry Hudgins and Dean Patterson

Lincoln, Nebraska

December, 2010

DESIGN OF AN INTEGRATED-STARTER ALTERNATOR FOR A SERIES HYBRID ELECTRIC VEHICLE: A CASE STUDY IN AXIAL FLUX PERMANENT MAGNET MACHINE DESIGN

Jessica Lynn Colton, Ph.D.
University of Nebraska, 2010
Advisors: Jerry Hudgins and Dean Patterson

This thesis details the design of an electric machine to perform as both a starter and alternator in a series hybrid electric vehicle. The focus of the work is on practical design aspects specific to single-sided axial flux permanent magnet machines with non-overlapped windings. First, a characterization of the rotor losses in these machine types is presented through experimental validation of finite element analysis estimates. The approaches taken to model the axial flux geometry, especially in two-dimensions, are detailed, and the difficult issue of validating the finite element analysis estimates with experimental data is addressed with a prototype 24-slot, 20-pole single-sided machine fitted with single-layer non-overlapped windings. Next, the comparative advantages and disadvantages of the single-sided axial flux geometry and the most common form of radial flux structure, with an inside rotor, are explored within the context of surface mount permanent magnet machines. New material is offered which highlights the benefits of the single-sided axial flux geometry and the constraints and assumptions made when making the comparisons are discussed in detail, including a study of the biases these can introduce. The basis of comparison is founded on constant electromagnetic airgap shear stress, being the product of electric and magnetic loading, and indeed the constancy of both those factors. The metrics used for comparison are the mass of the active materials and the volume essential to house said materials. A range of lesser issues that are relevant when choosing a machine structure are presented and discussed. Finally, the performance criteria for the integrated starter-alternator are quantified based on characterization of the internal combustion engine and the energy storage system of the vehicle and a full account of the design process is detailed, including justification of all design choices.

Acknowledgement

First and foremost, I would like to thank my advisors, Prof. Jerry Hudgins and Prof. Dean Patterson, for their unwavering support and guidance in all the technical and personal aspects of my studies.

I would also like to thank the other members of my committee, Prof. Annete Mÿetze, Prof. Wei Qiao and Prof. George Gogos, for their valuable comments on and corrections to my dissertation document as well as their assistance throughout the process of my Ph.D. work.

I wish to thank Paul Marxhausen, Tom Grady and James Nau for their technical assistance during the course of my project. Additionally, I am grateful to all of my colleagues in the Energy Systems Laboratory for their friendship and technical insight.

Special thanks are due to Fasco Australia P/L for permission to publish parts of this work.

Finally, I am indebted to my husband, Michael Hammons, for his steadfast support throughout these demanding years and to my son, Logan, who has already given me a new-found motivation.

Contents

List of Figures

List of Tables

Symbols and Abbreviations

A_e	electric loading
AF	axial-flux
A_g	airgap surface area
A_s	total slot surface area
B_g	airgap flux density
B_m	magnetic loading
B_r	magnetic remanence
BSFC	brake-specific fuel consumption
B_t	steel flux density
DL	double-layer
FEA	finite element analysis
ff	fill factor
GCD	greatest common divisor
h	model depth
HEV	hybrid-electric vehicle
I	RMS value of the stator current
ICE	internal combustion engine
ISA	integrated starter-alternator
J	current density
l_a	machine axial length
l_e	winding end-turn length (radial direction)
l_g	airgap length
l_m	magnet thickness
l_r	rotor thickness used magnetically
l_s	slot depth
l_y	stator yoke thickness
m	symmetry multiplier
N_c	number of coils per phase
NOW	non-overlapped winding
N_s	number of stator slots
N_t	number of turns per coil

p	number of rotor poles
P	number of poles per meter
P_e	electrical power
P_{f+w}	friction and windage loss
PM	permanent magnet
P_m	mechanical power
P_r	rotor power loss
$P_{r,NOW}$	rotor loss due to NOW
$P_{r,slot}$	rotor loss due to stator slotting
$P_{s,Cu}$	stator copper loss
$P_{s,Fe}$	stator iron loss
Q	number of slots per meter
r_{av}	average radius
r_i	inner radius
RF	radial-flux
r_o	outer radius
SA	surface area
SL	single-layer
s_{pp}	slots per pole per phase
TD	torque density
w_s	slot width
w_t	tooth width
V_{cu}	copper volume
V_{mag}	magnet volume
V_s	steel volume
V_{pack}	package volume
α_{asp}	aspect ratio
α_{SR}	split ratio
δ_{rad}	wasted fraction of rotor volume in RF machines
θ_m	magnet pole arc
θ_p	pole pitch
υ	harmonic number
σ	airgap shear stress
σ_e	conductivity

$\boldsymbol{\tau}$	torque
$\boldsymbol{\phi_{pole}}$	flux per pole

Chapter 1

Introduction

Interest in hybrid-electric vehicles (HEV) in the US has been growing significantly over the past decade, primarily as a result of rising fuel costs and environmental and sociopolitical concerns about oil consumption. The HEVs on the market today are primarily parallel (or *mild*) hybrids in which the drive power for the vehicle is supplied by both an internal combustion engine (ICE) and a set of electric machines. A different, and arguably more efficient, system design is the series HEV, or *strong* hybrid, in which the ICE is disconnected from the drive-train and all drive power is provided to the wheels through the electric machines. A conceptual schematic of this system, with an additional plug-in charging option, is shown in Fig. 1.1. A main result of the ICE disconnection is that the engine now has the flexibility to be run at its most fuel-efficient operating point without affecting the drive profile of the vehicle. The project on which this dissertation is based entails the conversion of a parallel HEV to a series HEV through a redesign of the energy storage system of the vehicle (Fig. 1.1).

The focus of this paper is the design of the electric machine that will perform as the generator shown in Fig. 1.1. It should be noted that this machine must also have the ability to operate in motoring mode to provide mechanical power to the ICE during startup; thus, the machine will herein be referred to as an *integrated starter-alternator* (ISA). The concept of an ISA is not a

new one, and with the growing peripheral electrical demands, even in traditional gasoline-engine vehicles, the design of more efficient and higher power alternators has become an important research topic.

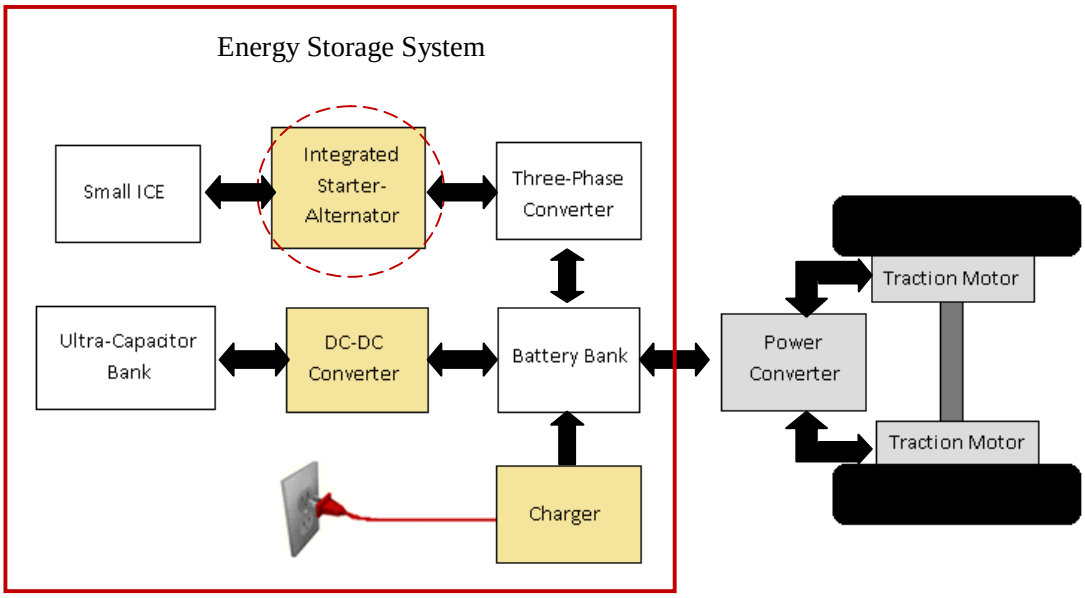

Fig. 1.1. Conceptual schematic of a series HEV system.

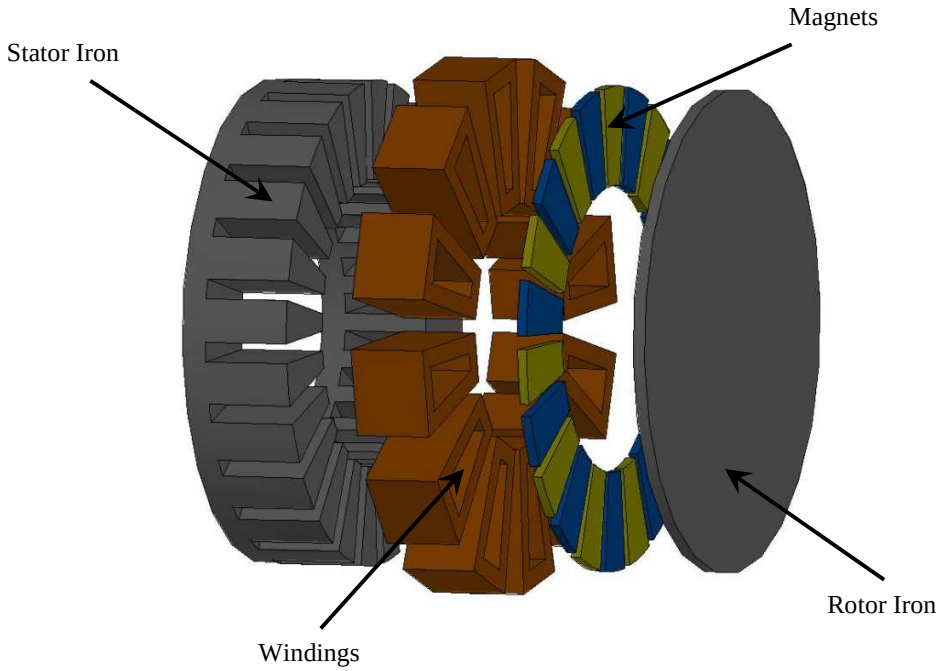

Fig. 1.2. Basic structure (active materials) of a single-sided AF PM machine.

1.1 Motivation of the Work

In the context of the aforementioned project, this dissertation is based on several aspects of electric machine design with a focus on the single-sided axial flux (AF) permanent magnet (PM) machine geometry (Fig. 1.2). AF geometries are not new. Faraday's first machine in 1831 was an axial flux machine and Tesla patented a disk motor in 1889. This geometry has always appealed to innovative thinkers in electric machines, but has been dogged by some extra difficulties in arranging the mechanical structure. This trouble was primarily in accurately maintaining a necessarily small airgap in a relatively large disk-shaped machine. Thus, while many people have researched AF induction machines, they have not, in general, proved economic to manufacture because of the substantial benefit of a very small air-gap in an induction machine.

The advent of rare-earth PMs has, however, made machines designed with rather larger air-gaps perfectly feasible. It is likely that this single fact has brought the AF machine back into purview. When efficiency is of concern, the use of PMs in a machine hardly requires justification, especially as the cost of rare-earth PM material has become more reasonable in the last decade. The most widely used PM material in electric machines is NdFeB because of its high energy product, residual flux density and magnetic coercivity in comparison to other magnetic materials. Further rationalization of the choice to design this ISA as a PM machine using NdFeB as the field excitation is both redundant and unnecessary.

Given all of this, the current reality is that while much research is carried on in universities regarding AF machines (a recent machines and drives conference had 262 papers with "machine" in the title, 14 of these had "axial flux" or "axial gap" in the title), they have not yet entered into the marketplace at anything like this frequency of occurrence, appearing only in applications where the aspect ratio is a dominant consideration, such as in-wheel vehicle drives. One goal of this research is to provide a comparison of the single-sided AF machine geometry with the more traditional, inner-rotor, radial flux (RF) machine structure in order to demonstrate the viability of this type of machine.

Finite element analysis (FEA) is an important design tool that is used extensively in the field of electric machine design. Two-dimensional (2D) modeling is often preferred over its three-dimensional (3D) counterpart due to reduced complexity in the modeling and appreciably decreased computation time and resources. However, unlike the RF geometry, the AF machine is a naturally difficult structure to model in 2D. If this is in fact managed, there are inherent errors in the model due to the necessary geometrical approximations. A second goal of this research is

then to compare machine performance results obtained via FEA in both 2D and 3D with actual experimental data from a test machine using rotor loss calculation (or measurement) as the basis of comparison.

In recent years, the use of non-overlapped winding (NOW) schemes in which a coil spans a single tooth as shown in Fig. 1.3, has largely replaced that of traditional full-pitched windings in high performance electric machine designs. A discussion and brief tutorial of the theory behind NOW is provided in Appendix B. Inherent in these winding designs are many benefits including reduced copper mass (and loss), better machine manufacturability, decreased cogging torque and performance enhancements in terms of fault-tolerance and flux-weakening capabilities, just to name a few. However, the use of NOW also comes with penalties resulting from a harmonic-rich airgap MMF waveform that manifests as reductions in winding factors and increased rotor losses when compared with machines equipped with traditional windings. Thus, the final goal of this work is to characterize the rotor losses in single-sided AF PM machines fitted with NOW through the difficult issue of validating FEA estimations with experimental data.

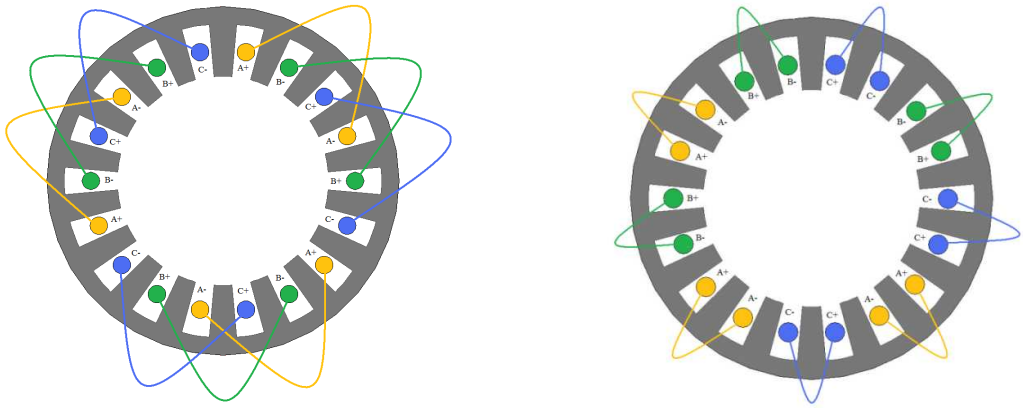

(a) **(b)**

Fig. 1.3. Examples of stator windings for a RF, three-phase (a) conventional winding (18-slots/6-poles) and (b) a single-layer NOW scheme (18-slots/22-poles).

1.2 Scientific Contributions and Relevant Publications

The scientific contributions of this work are summarized as follows:

1. A comparative study on AF and radial-flux (RF) PM machine geometries is done with a focus on the single-sided AF structure. (Chapter 3)

2. An assessment of 2D and 3D FEA modeling of single-sided AF PM machines is provided including measurement of rotor loss and comparison with FEA results. (Chapter 2)
3. A detailed account of the machine design process for the ISA application is given with a focus on details specific to the design of single-sided AF PM machines. (Chapter 4)

Publications associated with this dissertation are:

1. J. Colton, D. Patterson, J. Hudgins, "Rotor Losses in Axial-Flux Permanent-Magnet Machines with Non-Overlapped Windings", IET *Conference on Power Electronics Machines and Drives*, Apr. 2010. *(Currently in re-write process for submission to IEEE Transactions.)*
2. J. Colton, D. Patterson, J. Hudgins, K. Vacha, "Generator Design for Existent Windmills: From Water Pumping to Electricity Generation", IEEE *Syposium on Power Electronics, Machines and Drives in Wind Applications*, Jun. 2009.
3. D. Patterson, J. Colton, B. Mularcik, B. Kennedy, S. Camilleri, R. Roboza, "A Comparison of Radial and Axial Flux Structures in Electrical Machines", IEEE *International Electric Machines and Drives Conference*, May 2009. *(Currently in submission process for IEEE Transactions.)*
4. J. Colton, D. Patterson, J. Hudgins, "Design of a Low-Cost and Efficient Integrated Starter-Alternator", IET *Conference on Power Electronics Machines and Drives*, Apr. 2008.

1.3 Literature Review

This literature review is divided into three topics of interest: a historical development of the theory behind NOW, preceding work done on the impacts of NOW implementation on rotor eddy current losses and previous research involving comparisons between AF and RF machine structures. The aim is to provide an account of the state of the art in the technical fields relevant to the research work presented in this dissertation.

1.3.1 Non-Overlapped Windings

For the past decade, much attention has been given to winding schemes where the stator coils wrap around a single tooth, in contrast with the conventional windings in which the coils span three teeth (Fig. 1.3). These new types of windings have been called many names, "fractional-slot" or "concentrated" windings for example, but will be termed "non-overlapped" windings

(NOW) throughout this paper. NOW can either be described as double-layer (DL), in which there is a coil is around every tooth, or single-layer (SL), where there are only coils placed around alternating teeth as shown in Fig. 1.4 for an AF stator. The subsequent literature review is an attempt at a coherent description of the major advances in NOW analysis and design.

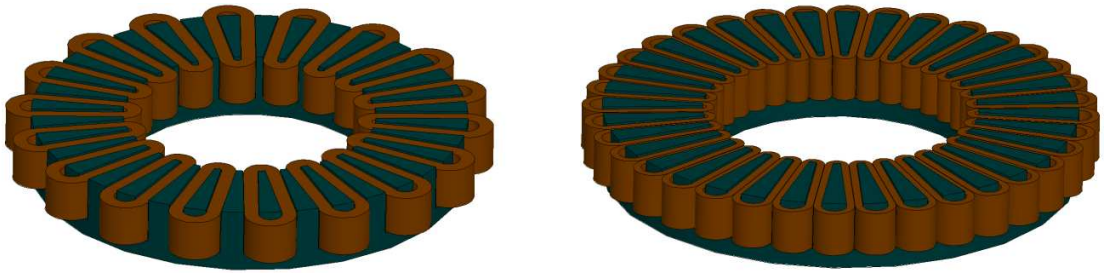

(a) **(b)**

Fig. 1.4. Illustration of (a) SL and (b) DL winding layouts on an AF machine stator.

Cros and Viarouge (2002) presented a study of three-phase NOW machines with various slot-pole combinations. One outcome of the study was the identification of which slot-pole combinations, for slot numbers less than 24, allow for a NOW and whether a SL layout can be used. More importantly, the winding factor, which gives insight to the machine performance, was computed for each structure. Several specific structures were compared, including FEA calculation of their torque output waveforms, and Cros and Viarouge concluded that the best machine performance is obtained when the number of slots per pole per phase (s_{pp}) is between *1/3* and *1/2*. Particular attention was given to the 12-slot/10-pole SL winding structure for its low torque ripple and minimal cogging torque.

Magnussen and Sadarangani (2003) added to work of Cros and Viarouge (2002) by identifying additional structures that can support NOW and detailing the analytical derivation of the winding factor computations. This was accomplished by showing that the airgap MMF waveforms of NOW machines have significantly increased harmonic content as compared to a machine with unity s_{pp}. It is this inherent increase in MMF harmonics that has prompted much of the continuing research into the characteristics of NOW machines.

A comprehensive study of NOW machines was presented by Salminen (2004). Winding factors and harmonic components were calculated for different slot-pole combinations and the characterization of cogging torque, torque ripple and inductances were performed analytically and verified via 2D FEA. A prototype 12-slot/10-pole *45 kW* RF internal permanent-magnet (IPM)

machine with DL NOW was constructed to validate the expectations resulting from the analytical techniques and FEA. Good correlation was observed.

Ishak et al. (2006) incorporated both analytical and FEA techniques in the investigation of machines which can support either a SL or DL NOW to identify the positive and negative aspects of using one layout over the other. One result of the work is that both the winding factor and the self-inductance corresponding to a SL winding may be higher than those for the equivalent DL scheme. Additionally, it was shown that the mutual-inductance between phases is lowered when a SL winding is employed for a given slot-pole combination. The implications of these findings prompted further investigations into the use of NOW machines for applications that require field-weakening capabilities or where fault-tolerance is of paramount importance.

Building on the idea of using NOW machines for fault-tolerant applications, Bianchi et al. (2005, 2006) applied the use of an analysis and design method, called the star-of-slots, to NOW machines. This method is used to present a graphical (phasor) representation of the effects of different order harmonics by characterizing the EMF (or MMF) contribution for each individual harmonic. More importantly, this method represents a simple, practical approach to designing the physical layout of the windings in a NOW machine by applying the star-of-slots method to the main harmonic. Bianchi et al. also evaluated the self and mutual inductances of both SL and DL winding schemes for machines with several slot-pole combinations, with results in accordance with those described by Ishak et al. (2006).

El-Refaie et al. (2005, 2006) offered closed-form techniques to analyze various parameters of NOW machines whereas previous work had been primarily based on FEA. Analytic expressions were presented for calculations of the open-circuit magnetic field and back-EMF waveforms, resistance and inductance of the windings, and torques for both normal and flux-weakening modes of operation. The developed analytical techniques were applied to a 36-slot/42-pole test machine and the resulting calculations were verified via 2D FEA.

Several authors have investigated the mechanical characteristics of certain NOW schemes. Wang, et al. (2006), identified a type of NOW scheme (called *modular*) in which coils of a particular phase appear in groups. These (RF) machines are shown, via analytical techniques and experimental verification, to exhibit a harmonic-rich radial force density pattern, raising the likelihood of low-frequency vibration excitation during normal operation. Dorrell et al. (2008) studied the effect of different rotor eccentricities on surface-mount permanent magnet (SMPM)

NOW machines with sinusoidal excitation. Unsurprisingly, through both an analytical algorithm and FEA, it was found that unbalanced magnetic pull was more prominent in the so-called *modular* machines due to the asymmetry inherent in the windings.

The studies described up to this point in the literature review have primarily focused on application of NOW to RF machines; however, it has been shown that these winding schemes are also beneficial for AF machines. Kamper et al. (2008) detailed the use of NOW for an air-cored AF machine. The analytical winding factors for iron-cored AF, NOW machines were investigated and used to develop complementary expressions for corresponding air-cored machines. Experimental data was offered to support the analytical work and verify that for an air-cored AF machine, NOW can provide better performance than a traditional distributed winding.

Given the advantages of NOW over traditional winding schemes described throughout the literature, it is justified for NOW to be employed in the design of the AF PM machine for the ISA application which is the focus of this paper. However, it should be noted that the study of the impacts of NOW in machines has not been exhausted. One area, in which there is still need for research, is with regards to the impacts of the space-harmonic content of the airgap MMF waveform on rotor losses as is detailed in the next section.

1.3.2 Rotor Eddy-Current Losses

The computation of rotor losses in PM machines has gained interest recently due to the increased implementation of NOW schemes in machine design. It has been shown that NOW induce rich harmonic content in the airgap MMF distribution. These harmonics, by definition, rotate at speeds and directions which are not synchronized to the rotor rotation (the main MMF harmonic), and therefore a time-varying flux pattern is introduced in the rotor materials and eddy-current losses there are increased. Efforts in describing and defining these losses have primarily been concentrated in the last several years as will be illustrated here.

Bianchi et al. (2010) calculated the rotor losses due to MMF harmonics of RF NOW machines by using analytical techniques to simplify a 2D FEA procedure. The stator-induced harmonics were transformed into a rotor reference frame frequency and applied to current sheets in the model. The rotor losses for an extensive list of slot-pole combinations for a particular machine size were tabulated and the main result was that the SL winding schemes exhibit increased loss due to richer harmonic content, especially sub-harmonics, than their DL counterparts. It should be noted

that the effects of stator slotting and any time-harmonics in the stator current waveform were neglected.

Saban and Lipo (2007) introduced a method of calculating rotor eddy-current losses for a high-speed RF machine in which both 2D and 3D FEA were employed. The main idea of the technique is that 2D FEA can be used to determine a rotor-referenced current sheet, which mimics the effects of the stator MMF waveform, to serve as an input to a 3D model. The method presented takes into account time harmonics, space harmonics and the effects of slotting in the MMF distribution, however, no loss calculation results were presented.

An analytical technique for calculating rotor back-iron eddy-current losses due to MMF space harmonics in a RF machine was presented by Polinder et al. (2007) in contrast to the FEA methods that had thus far been developed. The technique is based on decomposition of the MMF distribution (with slotting incorporated by application of Carter's coefficient) into its harmonic components and calculating the corresponding individual flux density magnitudes to be used in the loss calculations. Jassal et al. (2008) used this approach to compare rotor back-iron loss between three different NOW machines and a machine with traditional windings, confirming that the rotor loss for the NOW machines all exceed that of the traditional machine.

Han et al., (2010) examined rotor eddy-current losses for an IPM machine using a similar approach as was suggested by Polinder et al. (2007); except that here the loss calculation was performed via 2D FEA. The study identified that the parameters with the greatest impact on these losses are the magnitude of the fundamental component of the stator MMF, the stator slot pitch and the yoke pitch between the rotor barrier ends.

Nuscheler (2008) presented a 2D analytical model for calculating rotor eddy-current losses, in a RF SMPM machine, which is derived directly from Maxwell's equations. Multiple instances of two different slot-pole combination machines, each with varying degrees of rotor lamination and magnet segmentation, were analyzed with the model in terms of only the harmonic with the highest magnitude (excluding the main harmonic). It was determined that lamination of the rotor yoke increases the eddy-current losses in the magnets, but that loss can be mitigated by segmentation of the magnets.

A study involving experimental validation of analytical rotor eddy-current calculations for an AF machine was performed by Alberti et al. (2008). The analytical method is based on solutions of Maxwell's equations in two dimensions and the losses are calculated by considering the

contribution of each harmonic individually. The authors were careful to include the effects of stator slotting, as AF machines typically employ open slots. An experimental procedure was proposed in which the rotor eddy-current losses are calculated via a power balance and good correlation between the analytical and experimental results was observed.

Yamazaki et al. (2008) described their work involving the use of proprietary 3D FEA software to calculate rotor losses in both IPM and SMPM RF machines fitted with either NOW or conventional distributed windings. The FEA algorithm was verified experimentally by comparing torque and iron loss calculations (including both hysteresis and eddy-currents) to those obtained from measurements taken from an operating machine by a simple power balance. The primary results of the investigation are that the eddy current losses in a PM machine with NOW are much larger than that of an equivalent distributed winding machine and that the primary magnet eddy current loss in an SMPM machine is a result of stator slot openings.

1.3.3 Machine Geometry Comparisons

The difficulty of making comparisons between machine geometries is bound up in the issue of attempting to compare apples with apples. Thus various constraints are imposed by researchers to try and force equality in comparison. The end result is often that the constraints themselves favor one geometry over another, leading to inconclusive results. The general message of the literature that will be presented is fairly clear: Researchers have demonstrated that at a high pole count, and if the aspect ratio is free or constrained to large values, any of the AF geometries should be seriously considered as a design option.

In the first paper we study, Zhang et al. (1996) laid out a comparison of the standard inside rotor radial flux geometry with three kinds of axial flux geometries, denoted AFPM-11 (one stator, one rotor), AFPM-12 (one stator, two rotors) and AFPM-21 (two stators, one rotor). The two kinds of AFPM-12 machines, which have also been termed TORUS machines and are discussed in detail by Huang et al. (2001), were not separately considered. In one of these, magnet poles of the same polarity face each other across the stator and the machines are known as TORUS-NN types; whereas in the other, opposite polarities face each other and are known as TORUS-NS machines. For clarification, the AFPM-12 studied by Zhang et al. (1996) is a TORUS-NN type. Further research, as will be discussed subsequently, has shown that using slotted or non-slotted stators can add more possibilities to the range of axial flux machines, and indeed, the TORUS-NS type can be constructed with no stator iron.

The work reported by Zhang et al. (1996) was based on the well-known sizing equations involving electromagnetic shear stress, where specific torque, or torque-per-unit-mass, was derived. An advantage for AF machines that increased with pole count was demonstrated. The geometric study appears not to have included the volume associated with providing the electric loading which will be included in later sections. Two RF and three AF designs were compared and the results suggested that, when compared with the best RF design, the AFPM-11 was better (by measure of specific torque) by a factor of 1.8, the AFPM-12 by a factor of 2.1 and the AFPM-21 by a factor of 2.4.

Huang et al. (1999) reworked the sizing equations with much more detail, comparing the AFPM-12 with a TORUS-NN machine. No direct comparison of RF and AF structures was covered; however, it was observed that a PM axial flux machine has a significantly lower volume than an equivalent squirrel cage induction machine.

Simsir and Ertran (1999) looked specifically at the TORUS-NN machine in comparison with a traditional RF machine for a particular application. The conclusion was that the AF brushless DC motor has a much higher specific torque than the RF brushless DC motor and that this advantage increases with higher pole counts.

The standard RF geometry and four different AF geometries were studied by Sitapati and Krishnan (2001). The AF structures included a single-sided layout (i.e. AFPM-11) with both slotted and slotless stators considered, the dual stator AFPM-21 and a variant on the TORUS-NS machine in which the single stator had no iron to encase the windings. Detailed designs of all five machines were carried out at five different power levels, with the aim of producing similar performances and efficiencies. The conclusion was that the AF machines always have a smaller volume than the RF machines for a given torque rating. It was also noted that the slotless designs required more copper and magnet material than the other geometries, which would impinge on overall cost.

Cavagnino et al. (2002) studied, primarily from a thermal standpoint, the RF machine and the AFPM-21 machine. This paper goes into a very high level of detail, but ultimately only designs that ensured a wasting surface that was adequate for the losses generated were considered. Designs were carried out for a range of aspect ratios, or diameter/length (D/L) ratios, and showed very high specific torque in buildable AF machines at large aspect ratios. In general, an AF machine design with a small aspect ratio is not practical.

A three-way comparison between RF, AF and transverse flux motors was conducted by Rahman (2004), with the specific application of an in-wheel motor for an electric vehicle. The comparison is based on a patented “twin pole” winding scheme and is made based on physical size (i.e. package dimensions) for a 9 pole-pair machine with five phases. The RF and transverse flux motors were both configured with the rotor outside the stator and the AF machine considered is a single-sided structure. The results showed that the RF motor had a slightly better performance than the AF motor. The transverse flux version demonstrated the best performance, though it was designed with 20 pole pairs because the model would not converge with 9 pole pairs. The constraints for this comparison included not only a fixed pole count but also a given package size. Rahman does state that the AF motor would exceed the performance of the RF design if the aspect ratio was greater than 5, whereas for this comparative study, the packaging dictated an aspect ratio of 3.5. Rahman also reports that the cogging torque was lower for the AF design.

Parviainen et al. (2005) reported a detailed study comparing the traditional RF geometry to the AFPM-21 structure. Mechanical constraints were discussed and included in the analysis. The metric of comparison was solely the cost of the active materials. The conclusion was that at 8 poles, the two designs were of similar cost, but for designs with greater than 8 poles, the AF geometry was lower cost than the radial flux.

Chapter 2

Rotor Losses in Axial Flux PM Machines

The goal of this chapter is to detail the process of using FEA (both 2D and 3D) to estimate the rotor eddy-current loss in a single-sided AF PM machine as well as to substantiate the FEA estimations with experimental measurements. While eddy-current rotor loss in an AF PM machine may not have as much impact on performance as that in say, an inner-rotor RF PM machine, the topic is still of concern because AF machines are typically designed with open slots and solid steel back-plates in addition to the possibility of using NOW.

The focus placed here on experimental measurement of these losses may initially seem frivolous in this age of rich computing resources and intelligent FEA software; however, this experimental evidence that is important specifically when AF PM machines are considered. Unlike the more traditional RF geometry, AF machines are difficult to model in 2D and if this is done, there are inherent errors in the model due to geometrical approximations. It is possible to use 3D analysis; however this approach is substantially more time and resource consuming than its 2D counterpart, so it is often not a good option until a design has been more established. Additionally, 3D FEA computations are quite sensitive to meshing operations and time stepping (when a transient solver is used).

A useful approach to modeling the AF PM machine in 2D will be described subsequently and the experimental measurements are then used to typify the magnitudes of errors that can be expected from the model estimations in both 2D and 3D. The process of experimentally isolating the rotor loss measurements is not trivial and will occupy the majority of this chapter.

2.1 Finite Element Analysis

The software used in the analysis described here is Ansoft's Maxwell® where the transient solver is utilized in order to include the large-scale motion of the rotor passing over the stator slots. The results presented here have been computed for a 24-slot/20-pole single-sided AF PM test machine with single-layer NOW. The specific parameters of the machine match those of the machine on which experimental tests are performed and are described below in Table 2.1.

TABLE 2.1 Parameter Values of the AF PM Test Machine Used for Measurement and Estimation of Eddy-Current Rotor Losses

Parameter	Value		Parameter	Value
Rated Power	1 kW		*Slots (N_s)*	24
Nominal speed	3000 rpm		*Poles (p)*	20
Stator O .D.	110 mm		*Winding type*	Single-NOW
Stator I. D.	66 mm		*Phase resistance*	1.3 Ω
Stator height	25 mm		*Phase inductance*	6 mH
Magnet type	NdFeB-N35		*Rotor thickness*	4 mm
Magnet thickness	4 mm		*Airgap length*	1 mm

2.1.1 2D Modeling

An approach to model the AF PM machine in two dimensions is to view the machine from the side (Fig. 2.1) and model a small portion of the machine with translation motion of the rotor piece instead of rotation. However, the translation motion causes errors in the particular software used in this project; so as a work-around, we liken the AF machine to a small piece of a very large RF machine. In this way, we can assign rotation motion around a radius on the order of 100 m in order to "simulate" the intended translation motion. Depending on the slot (N_s) to pole (p) relationship of the machine, the model need only contain a fraction of the total geometry where the appropriate symmetry multiplier (m), equal to the GCD$\{N_a,p\}$, is applied to the model. The edges indicated in Fig. 2.1 are assigned master/slave boundary conditions, where based on the

winding function shown in Fig. 2.2, the relationship for this particular machine model is master = -slave. The output parameters of the FEA (i.e. torques, etc.) can easily be converted from the large RF machine reference frame to that of the smaller AF PM machine that is under consideration.

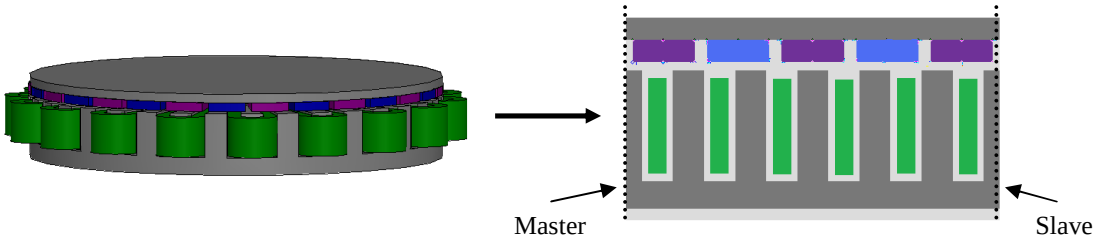

Fig. 2.1. Illustration of the 2D modeling of a single-sided AF PM machine.

In order to calculate the total eddy-current power loss in the rotor, the 2D FEA model is analyzed to determine the z-direction current density (J_z) in the magnets and rotor back-iron. The current density is used because the net current in each rotor component is necessarily zero (indeed it is forced to zero by a constraint in the model description). The rotor power loss (P_r) is then calculated as the integral over the model surface area (SA) as shown in (2.1) where h is the model depth in the z-direction ($h = r_o - r_i$) and σ_e is the conductivity of the material.

$$P_r = hm \iint_{SA} \frac{|J_z|^2}{\sigma_e} dSA \tag{2.1}$$

The analysis described was first conducted without a current input to the stator windings at various speeds in order to determine the rotor loss as a result of stator slotting alone ($P_{r,slot}$). Then, the same procedure was performed for rotor speeds of 1000 and 2000 rpm with stator current set to provide selected values of output torque to be consistent with the experimental operating points as described subsequently in section 2.2. Each simulation was carried out over a rotor rotation equal to one pole-pitch and calculation of rotor loss was made (by hand) at each of 10 time steps and then averaged to obtain the results shown in Table 2.2. It is these values that will be compared with experimental data.

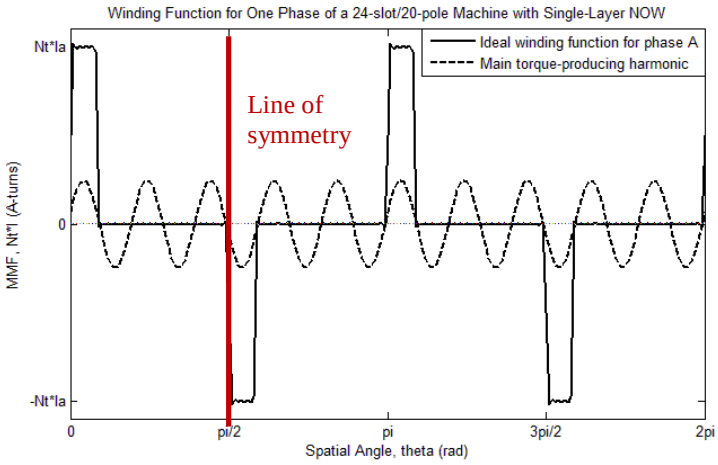

(a)

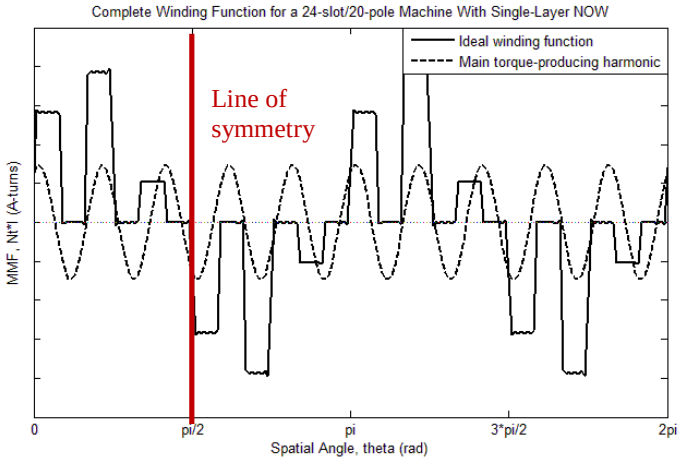

(b)

Fig. 2.2. Winding functions for the 24-slot/20-pole AF PM machine used for the measurement and estimation of rotor eddy-current losses. A single phase is shown in (a) while (b) shows the complete winding function for an arbitrary time instant.

TABLE 2.2 Rotor Loss Estimations Resulting from 2D FEA

Rotor Speed (rpm)	Output Torque (Nm)	Estimated Rotor Loss (W)
1000	0	1.8
1000	1.7	2.9
1000	2.7	4.4
2000	0	6.8
2000	1.7	10.1
2000	2.4	13.5
3000	0	14.8

2.1.2 3D Modeling

Some comparison of the 2D FEA estimations (and experimental measurement) of the eddy-current rotor loss for the test machine with what is expected to be more accurate estimations via 3D FEA was deemed useful. However, due to the complexity and time consumption of running a transient simulation in 3D FEA, somewhat limited results are presented here for comparison. Three full 3D simulations have been run to obtain values for $P_{r,slot}$ at speeds of 1000, 2000 and 3000 rpm. This was accomplished with a transient analysis in the aforementioned software employing large-scale rotor motion, but null currents in the stator windings.

It has been the author's experience in using 3D FEA that macroscopic calculations (i.e. torque) are quite robust, but more microscopic estimations (i.e. rotor loss) can be quite sensitive to solver parameters such as mesh and time step sizes. In fact, quite erratic (and physically impossible) results have been found with meshing that is too coarse and/or inappropriate time stepping. The eddy-current rotor loss estimations presented here have been obtained using the solver statistics detailed in Table 2.3 and though the symmetry rules applied in the 2D FEA are equally applicable here, the simulations were performed using the entire machine model. Each simulation was carried out over a rotor rotation equal to one pole-pitch and eddy-current loss calculations were made automatically at each of 100 time steps. The results of the 3D FEA estimations for the rotor eddy-current loss are shown in Fig. 2.3 with average values for $P_{r,slot}$ equal to 1.3 W, 5.7 W and 8.3 W for rotor speeds of 1000, 2000 and 3000 rpm respectively.

TABLE 2.3 Solver Parameters Used in the 3D FEA Calculation of Eddy-Current Rotor Loss

Parameter	Value
Magnet mesh	10,000 tetrahedra
Rotor back-iron mesh	10,000 tetrahedra
Stator pole-face mesh	5,000 triangles
Aspect ratio	3
Nonlinear residual error	0.001

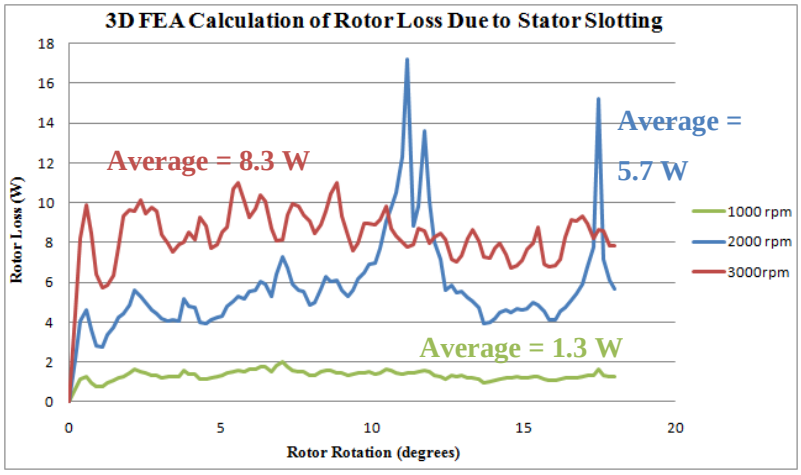

Fig. 2.3. 3D FEA calculation of $P_{r,slot}$ for rotor speeds of 1000, 2000 and 3000 rpm.

2.2 Experimental Measurement

The purpose of this section is to detail the experimental techniques used to isolate the rotor eddy-current loss. The methodology will be explained here, while the actual rotor loss determination (and comparisons with FEA calculations) will be addressed in the following section.

The test machine used for experimentation is a single-sided AF PM machine as pictured in Fig. 2.4 with parameters listed in Table 2.1. The problem of isolating the rotor loss is approached by running the test machine in generation mode via a drive motor, coupled through an in-line torque transducer. Rotational speed measurement is made using a Hall-effect sensor and both voltage and current measurements are accessible for all three phase outputs of the generator. The power balance for this described arrangement is given by

$$P_m - P_e = P_{f+w} + P_{Cu} + P_{s,Fe} + P_{r,slot} + P_{r,NOW} \tag{2.2}$$

where the power terms are:

P_m: mechanical power (input)
P_e: electrical power (output)
P_{f+w}: friction and windage loss
$P_{s,Cu}$: stator copper loss
$P_{s,Fe}$: stator iron loss
$P_{r,slot}$: rotor loss due to stator slotting

$P_{r,NOW}$: rotor loss due to NOW

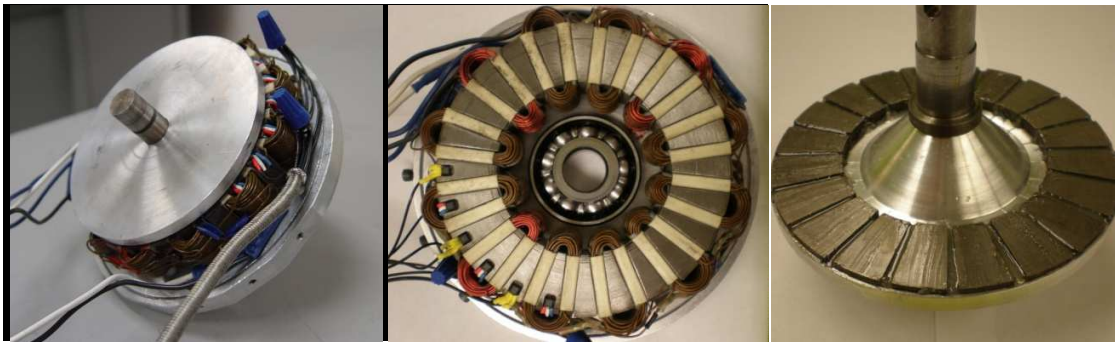

Fig. 2.4. Photographs of the single-sided AF PM machine used for experimentation.

2.2.1 No-Load Tests

The first no-load test is to determine the spinning loss in the test machine. This loss measurement encompasses P_{f+w}, $P_{s,Fe}$ and $P_{r,slot}$ and is accomplished through the setup described previously with the generator load disconnected. The measured spinning losses are shown in Fig. 2.5 for speeds in the range of 300 to 3000 rpm. In order to obtain the best resolution possible at no-load, the in-line torque transducer used in this setup is rated at only 0.5 Nm.

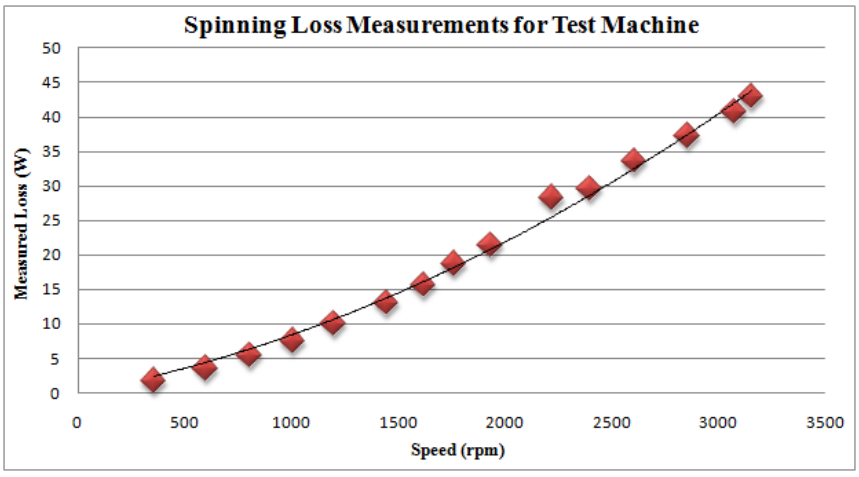

Fig. 2.5. Spinning loss measurements for the test machine shown with a 2nd-order polynomial curve-fitting for the actual measured data points indicated.

One concern that is often associated with single-sided AF PM machines is the large axial load experienced by the bearing. Therefore, the second no-load test performed was to isolate the bearing friction loss, P_{f+w}, as a function of speed (note that the aerodynamic portion of this loss is ignored). In order to do so, the spinning loss measurement previously described was repeated using an uncut steel toroid as the stator piece (still fitted with a Hall-effect sensor for speed measurement). The airgap was adjusted by adding shims between the bearing and the rotor brace such that the axial load in the bearing is equivalent to that of the actual machine, as computed via magnetostatic 3D FEA. Fig. 2.6 shows the results of the spinning loss measurements with the uncut toroid. It can be argued that this measurement also contains a core loss component, however, as can be seen in Fig. 2.7, the increased airgap reduces the magnetic penetration depth into the core and the flux densities encountered are quite small. Therefore any core loss here is considered to be negligible.

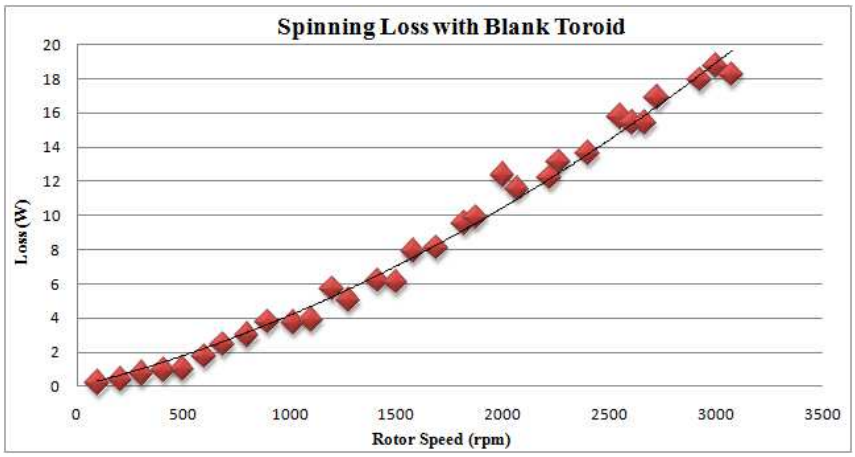

Fig. 2.6. Spinning loss measurements for the test machine where the stator is replaced with an uncut toroid shown with a 2nd-order polynomial curve-fitting for the actual measured data points indicated.

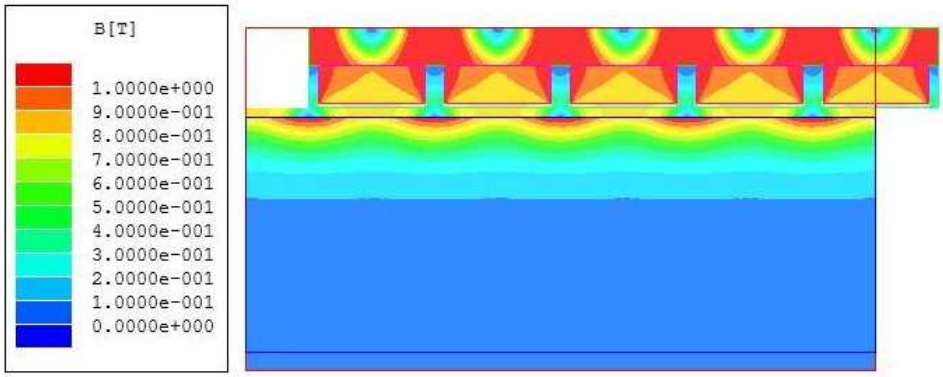

Fig. 2.7. 2D FEA representation of the stator flux densities present in the test machine when the stator is replaced with an uncut steel toroid.

2.2.2 Core Loss Measurements

Arguably the most challenging experimental measurement to isolate is the loss in the stator core. The stator of this particular test machine is constructed from a toroidal core consisting of tape wound 0.28 mm thick grade M4, grain-oriented silicon steel. In order to typify the behavior of the core loss under different operating conditions, the B-H curve of an uncut toroid was measured for a range of frequencies and magnetic induction levels.

The toroid was fitted with two sets of windings where the primary was connected to the output of an audio amplifier (driven with a sinusoidal signal generator) and the open-circuit voltage on the secondary circuit was directly measured and numerically integrated to obtain the flux density measurement. The specific core loss (W/kg) was then determined by numerical calculations on the B-H curve, scaled by the physical parameters of the toroid. This procedure was completed for frequencies ranging from 60 Hz to 500 Hz (corresponding to the fundamental frequency of the machine at rated speed) and induction levels from 0.6 T to 1.8 T. A sampling of the B-H curves is shown in Fig. 2.8 and the results of the loss calculations are given in Table 2.4.

The type of steel used in the stator of this machine is grain-oriented and the loss measurements described previously are made for flux in-line with the rolling direction of the steel. This is the true flux path in the stator back-iron of the machine; however, in the teeth, flux is pushed directly across the grain orientation and it is expected that the loss would increase in this case. According to Soinski (1984), the specific loss is increased by a factor of approximately 2.8 when the flux path is 90^{o} from the rolling direction; it is this value that is assumed for the core loss calculations.

TABLE 2.4 Experimental Core Loss Data for the M-4 Steel Toroid Used for the Test Machine Stator at Various Frequencies and Induction Levels

Freq. (Hz)	Induction Level (T)	Specific Loss (W/kg)		Freq. (Hz)	Induction Level (T)	Specific Loss (W/kg)
60	1.8	**1.47**		300	1.8	**17.28**
60	1.5	**0.90**		300	1.5	**10.27**
60	0.8	**0.26**		300	0.7	**2.28**
100	1.8	**3.05**		400	1.8	**28.61**
100	1.5	**1.84**		400	1.4	**15.37**
100	0.9	**0.71**		400	0.8	**4.35**
200	1.8	**9.75**		500	1.5	**24.41**
200	1.6	**7.09**		500	1	**11.04**
200	1	**2.96**		500	0.6	**4.85**

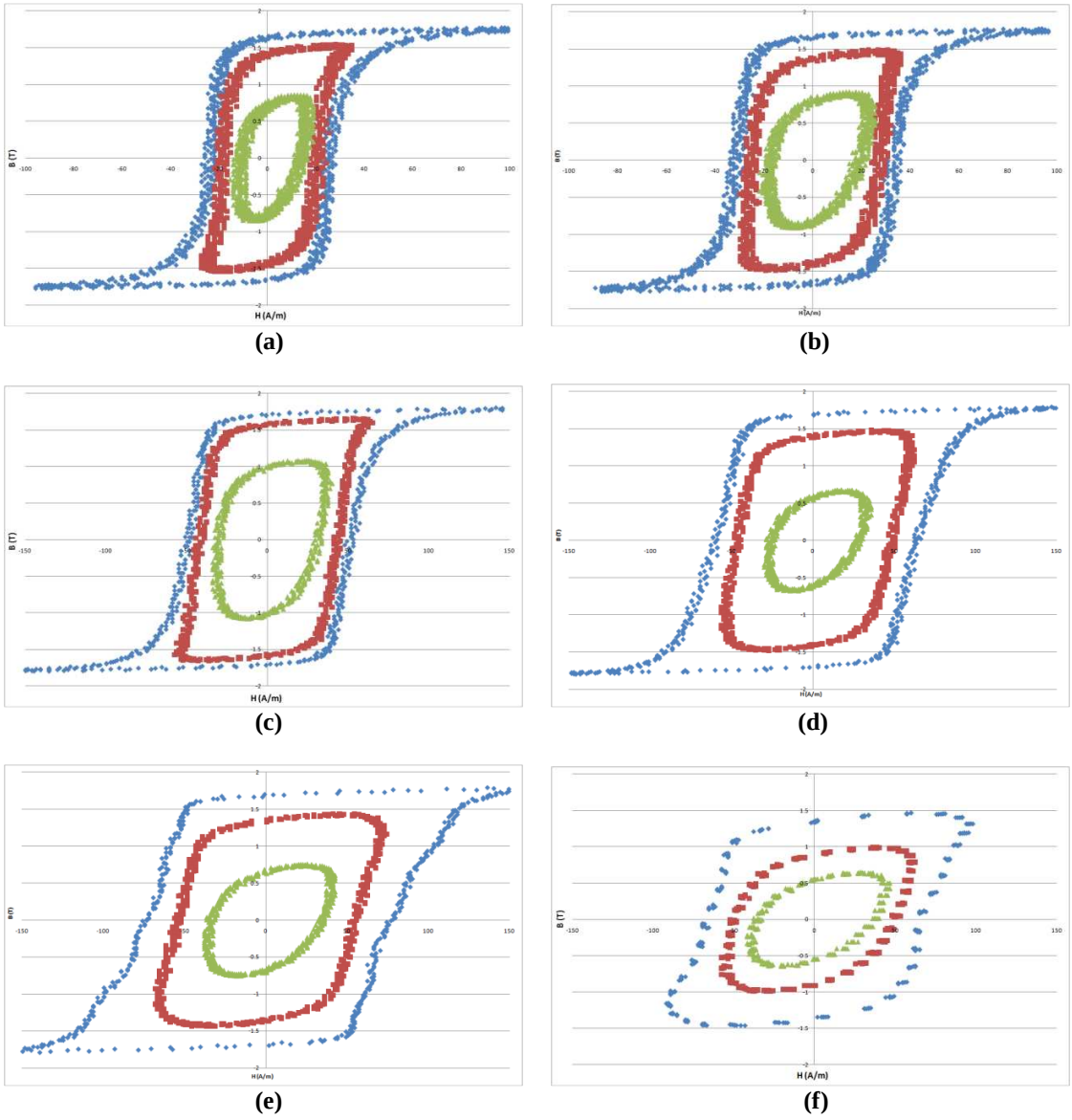

Fig. 2.8. B-H curves for the M-4 steel toroid used for the test machine stator at frequencies of (a) 60 Hz, (b) 100 Hz, (c) 200 Hz, (d) 300 Hz, (e) 400 Hz, (f) 500 Hz.

2D FEA was used to identify that the magnetic induction levels present in the stator teeth and yoke are 1.3 T and 0.8 T respectively. In terms of core size, the complete toroid has a mass of 1.15 kg where the total volumes of stator teeth and yoke are 41% and 20% respectively, of the uncut toroid mass. Thus, for loss calculations, the yoke mass is 0.23 kg and that of the teeth is 0.47 kg (total for all 24 teeth). Using this physical data, the total core loss in the machine can be calculated as a function of fundamental frequency (or rotational speed). To this end, the data given in Table 2.4 along with 2nd-order polynomial curve fits for each frequency as a function of

flux density was used to extrapolate values of specific loss at the induction levels of 1.3 T and 0.8 T. The core loss (in Watts) as a function of machine speed is then shown in Fig. 2.9.

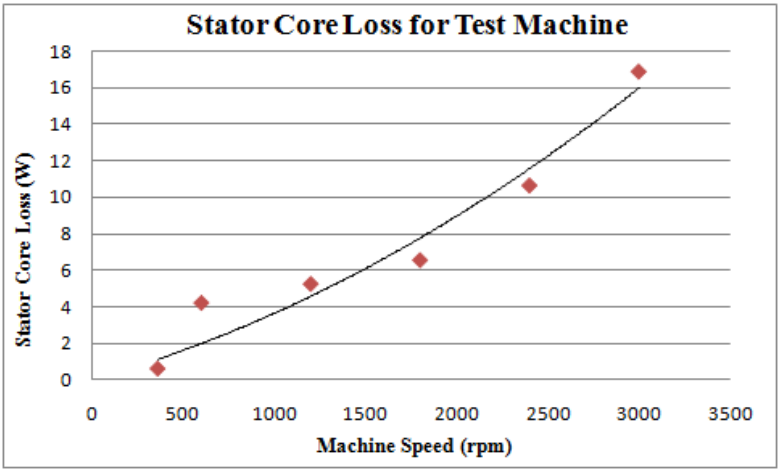

Fig. 2.9. Stator core loss for the test machine as a function of rotor speed. The points shown are not measurements; they are extrapolated from actual measurement data using a 2nd-order polynomial curve fit. A curve fit for the points shown is also illustrated on the graph, simply for the purpose of illustrating the trend of the calculations.

2.2.3 Loaded Tests

In these tests, the AF PM machine was run in generation mode, as previously described, with a variable resistance load connected and the resulting loss measurements are summarized in Table 2.5. The "Total Measured Loss" reported is the difference between the input P_m and the output P_e as described in (2.2). Simple i^2R calculations were made to determine the "Conduction Loss", where no discernible temperature rise was noticed in the stator windings.

TABLE 2.5 Summarized Results from Experimental Measurement of the Test Machine On-Load

Rotor Speed (rpm)	Output Torque (Nm)	Total Measured Loss (W)	Conduction Loss (W)
923	**1.7**	19.0	10.69
889	**2.2**	29.27	20.15
889	**2.7**	66.84	46.17
2000	**1.7**	46.92	10.86
2000	**2.3**	78.24	25.39
2000	**2.5**	93.22	31.63

2.3 Results and Discussion

In this section, the experimental rotor eddy-current losses ($P_{r,slot}$ and $P_{r,NOW}$) are inferred from the experimental measurements described in the previous section. Comparisons are also made with respect to the loss estimations obtained from FEA.

The rotor eddy-current loss that results from stator slotting alone ($P_{r,slot}$) can be isolated from the experimental measurements by subtracting the measured bearing loss (Fig. 2.6) and stator core loss (Fig. 2.8) from the spinning loss measurements shown in Fig. 2.5. The equations found from curve-fitting are used to evaluate the spinning loss and stator core loss at rotor speeds exactly corresponding to the measured data points of the bearing loss to provide the plot of $P_{r,slot}$ as a function of rotor speed shown in Fig. 2.10. Also shown on the plot are the estimations obtained via 2D and 3D FEA. It can be observed that the general shape of the data points from the 2D estimation is systematic, but the absolute values are quite overestimated. For the 3D estimations, the calculated values are in better agreement with the experimental results, but the trend of the curve appears non-physical, most likely as a result of the choices of mesh size and time steps in the computation process.

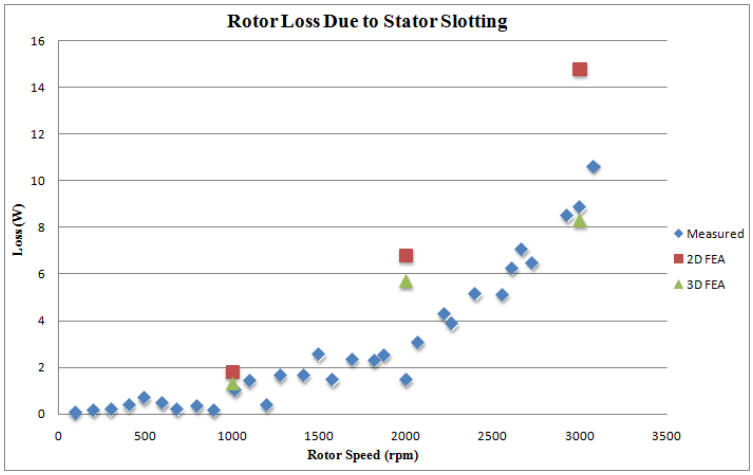

Fig. 2.10. Plot showing the relationship between $P_{r,slot}$ as inferred from experimental measurement and the estimated values obtained from 2D and 3D FEA.

The rotor eddy-current loss that exists as a consequence of the NOW scheme ($P_{r,NOW}$) is obtained from the experimental measurements of the machine on-load by subtracting the spinning loss (Fig. 2.5) and conduction loss (Table 2.5) from the total measured loss in Table 2.5. The equation found from curve-fitting is used to evaluate the spinning loss at rotor speeds corresponding to the

measured data points of the on-load testing. The results of this calculation are shown in Table 2.6 along with a reiteration of the 2D FEA estimations (3D FEA estimations of this value were not calculated due to the complexity and time consumption of running a full transient simulation in 3D).

The behavior (i.e. the trend) of $P_{r,NOW}$ both as inferred from experimental measurements and estimated via 2D FEA is as expected in that the loss increases as the current loading increases for a given rotor speed. However, the loss calculation based on experimentation increases at a drastically higher rate than is shown in the 2D FEA calculations. It is likely that this discrepancy is bound up in: (1) the number of measurements that must be taken when the machine is loaded in order to calculate $P_{r,NOW}$ and (2) the fact that the loss is so small in comparison with the total power output of the machine that large errors result from the subtraction of two relatively equal numbers. Further work should be done in the estimation of this value; however, because the measurement information is simpler to obtain, the trends for $P_{r,slot}$ shown in Fig. 2.10 give some insight into the differences between 2D and 3D FEA estimation for an axial flux machine.

TABLE 2.6 Comparison Between $P_{r,NOW}$ as Inferred from Experimental Measurement and the Estimations Obtained via 2D FEA

Rotor Speed (rpm)	**Output Torque (Nm)**	$\boldsymbol{P_{r,NOW}}$ **Measured (W)**	$\boldsymbol{P_{r,NOW}}$ **2D FEA (W)**
~1000	1.7	0.40	1.1
~1000	2.2	1.59	1.7
~1000	2.7	13.14	2.6
2000	1.7	12.46	3.3
2000	2.3	29.25	6.0
2000	2.5	37.99	6.7

Chapter 3

Machine Geometry

The purpose of this section is to provide a frank discussion of the comparative advantages and disadvantages of the single- and double-sided AF geometries as well as the inner-rotor style RF structure when considering surface-mount PM machines. The basis of the comparisons is founded on constant electromagnetic air-gap shear stress, being the product of electric and magnetic loading, and indeed the constancy of both of those factors. So also included in this section is a definition of electric and magnetic loadings in reference to the AF PM machine structure.

3.1 Electric and Magnetic Loading in Axial Flux Machines

The concepts of constancy of electric and magnetic loading need a little more care when applied to an axial flux machine as opposed to the more traditional radial flux structure. Because the ensuing comparisons are all made with assumptions of both constant electric loading and constant magnetic loading, the purpose of this section is to clearly characterize these in terms of the axial flux PM machine geometry shown in Fig. 3.1.

The airgap flux density, B_g (T), is established by the PM on the rotor in the axial direction and is assumed to have the ideal spatial distribution shown in Fig 3.2. The magnetic loading, B_m (T) is

defined here as the peak value of the airgap flux density waveform. It is dependent on the particular magnet material used in addition to the machine geometry and, assuming infinite permeability in the steel, can be determined from the relationship

$$B_m = B_r \frac{l_m}{l_m + l_g} \tag{3.1}$$

where B_r (T) is the magnetic remanence of the PM material and l_m and l_g represent the axial thickness of the magnets and airgap respectively. Carter's coefficient may be included in (3.1) if the effects of stator slotting are to be considered. It is assumed that the magnet pole arc, θ_m, is some arbitrary fraction of the pole pitch, θ_p, and that the ratio θ_m/θ_p is constant with radius. It should be apparent that under these assumptions, the magnetic loading of the axial flux PM machine does not vary with radius.

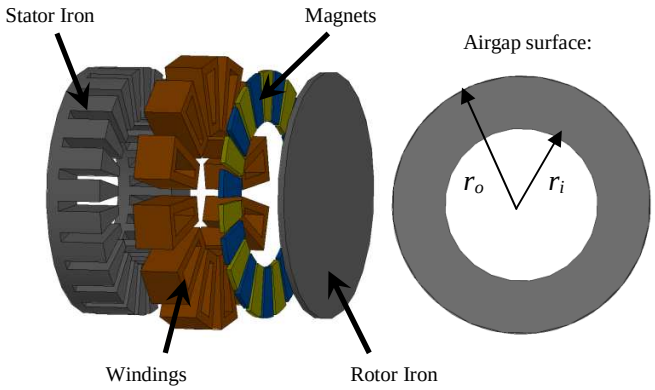

Fig. 3.1. Illustration of the active components and structure of a single-sided axial flux PM machine.

In a general sense, electric loading, A_e (A/m), is defined as the ratio of the total stator current to the machine circumference at the airgap interface (Miller, 1989). Now in an axial flux machine stator, the slots obviously fan out as seen in Fig. 3.1. These slots are also invariably of constant width, and hence of constant total current. Thus the electric loading, seen in the micro, is actually higher at the inner radius and lower at the outer radius. Without loss of generality, we use the average electric loading, defined at the average airgap radius, r_{av}, for a 3-phase machine as

$$A_e = \frac{6N_t N_c I}{2\pi r_{av}} \tag{3.2}$$

where N_c indicates the number of coils per phase, N_t denotes the number of turns per coil and I (A) is the RMS value of the stator current in any phase.

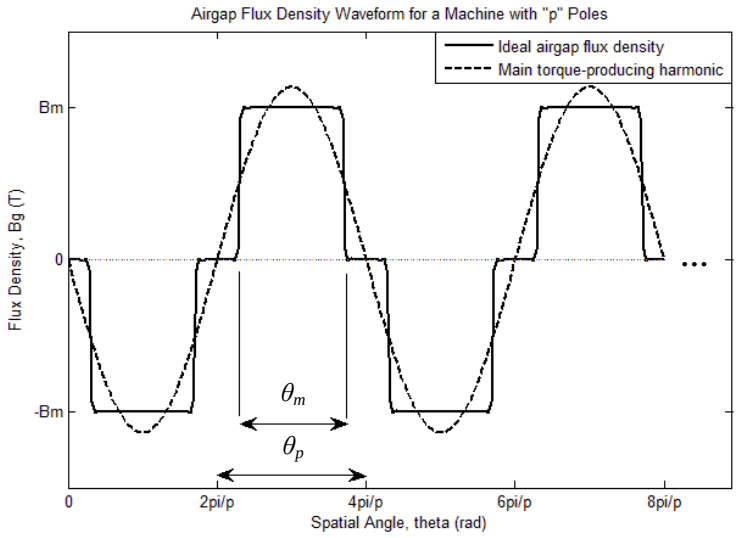

Fig. 3.2. Ideal airgap flux density distribution along the circumferential direction.

The spatial distribution of stator current is dependent upon the specific slot and pole combination used in the machine. For example, the ideal winding function for a single phase of a 6-slot/4-pole machine with non-overlapped windings is shown in Fig. 3.3-a and Fig. 3.3-b shows the complete winding function of the machine, assuming a balanced set of 3-phase currents, evaluated at some arbitrary time instant. The winding function is not dependent upon the radius at which it is considered.

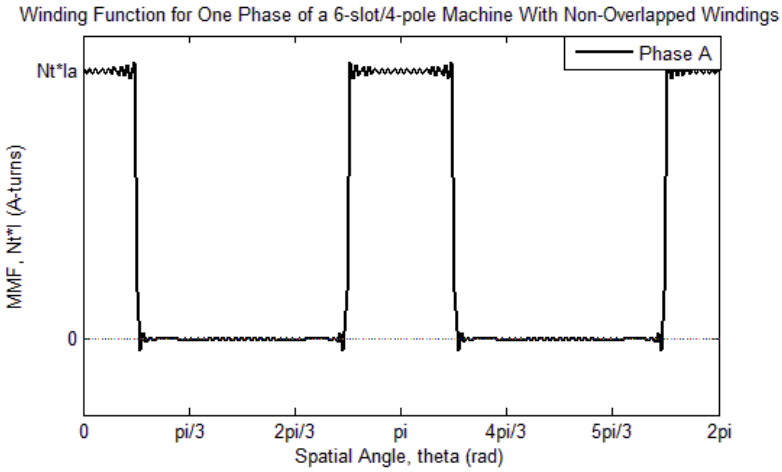

(a)

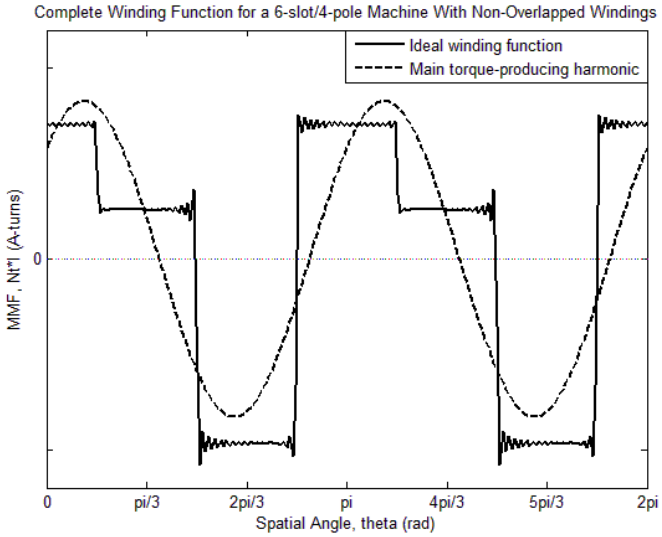

(b)

Fig. 3.3. Winding functions for a 6-slot/4-pole machine with non-overlapped windings. That of a single phase is highlighted in (a) where the two phases not shown are identical with phase shifts of 120^o and 240^o. In (b), the complete winding function for the stator MMF is shown for an arbitrary time instant.

Fundamentally, a force F (N) is produced in the machine due to the interaction of rotor flux and stator current. As detailed by Miller (1989), the electromagnetic airgap shear stress, σ (Pa) is defined as the magnitude of this force per unit airgap surface area and can also be expressed as the product of the electric and magnetic loadings as

$$\sigma = \frac{F}{\pi\left(r_o^2 - r_i^2\right)} = kB_m A_e \tag{3.3}$$

Specifically, only the spatial harmonics of the winding function waveform that coincide with those of the airgap flux density contribute to torque production. The proportionality constant, k, in (3.3) is used to account for the difference in magnitudes between the peak values of the ideal waveforms and those of the torque producing components as shown in Figs. 3.2 and 3.3-b. Finally, the torque, τ (Nm), produced in the single-sided axial flux machine shown in Fig. 3.1 can be defined in terms of the aforementioned quantities as

$$\tau = \sigma_{av} A_g r_{av} \tag{3.4}$$

where σ_{av} indicates the shear stress when the electric loading is evaluated at the average machine radius, r_{av} (m), and A_g (m^2) is the airgap surface area.

Since the slots in an axial flux machine are typically rectangular, of constant with (w_s) and depth (l_s) as shown in Fig. 3.4, it is reasonable to redefine average electric loading as

$$A_e = \frac{J l_s w_s N_s}{2\pi r_{av}} \tag{3.5}$$

in terms of the slot current density, J (A/m^2), usually established in design by thermal considerations. In this equation, N_s is used to represent the number of slots in the machine and the current density implicitly accounts for the slot fill factor. For the purpose of the subsequent discussions and comparisons, it is assumed that not only is the average electric loading kept constant, but so is the current density, in an effort to maintain the same order of loss in all the machine geometries under scrutiny.

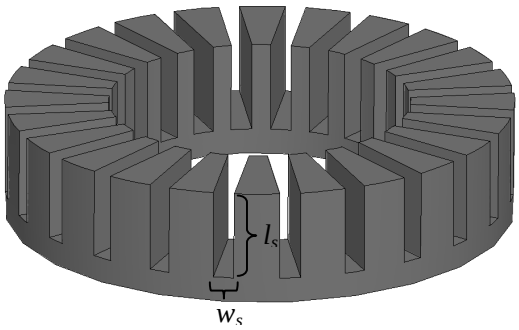

Fig. 3.4. Slot geometry in a typical axial flux machine stator.

The ensuing comparisons are made in terms of active material volume, so it is helpful to get a sense of how the dimensions of the machine may be impacted by the electric and magnetic loadings. The slot width is dependent upon the design choices of magnetic loading and the maximum flux density, B_t (T), allowable in the stator teeth and is given by

$$w_s = \left(1 - \frac{\theta_m}{\theta_p}\frac{B_m}{B_t}\right)\frac{2\pi r_{av}}{N_s} \tag{3.6}$$

Substituting (3.6) back into (3.5), it becomes clear that the slot length, which has a direct impact on the total axial length of the machine, is uniquely determined once the design parameters of electric and magnetic loading, current density and maximum steel flux density are defined. The expression for slot length is given by

$$l_s = \frac{A_e}{J}\left(\frac{B_t}{B_t - \frac{\theta_m}{\theta_p}B_m}\right) \tag{3.7}$$

3.2 Single- versus Double-Sided Axial Flux PM Machines

Only a minority of the studies discussed in the literature review considered the single-sided axial flux machine (Fig. 3.1). Those that did tended to make a comparison between single- and double-sided versions of a machine at the same radius. However, if a torque specification is known and the dimensions of the two competing machines are essentially free, then the single-sided machine can be shown to exhibit a significantly higher utilization of active material.

The subsequent development starts with a single-sided axial flux machine and the amount of active material is then doubled for two separate design cases, while maintaining constancy of both electric and magnetic loadings. In the first case, a double-sided machine (dual stator) is created at the same stator outer radius, while the second approach is to reallocate the additional active material to construct a larger, single-sided machine. The derivation shows a 41% increase in the torque (power) for the enlarged single-sided machine when compared with the double-sided version.

For the baseline single-sided axial flux PM machine shown in Fig. 3.1, the torque is defined as in (3.4). Following common usage when dealing with radial flux machines, we adopt the term split ratio, which is, neglecting the airgap, the ratio of the stator inner diameter to the stator outer diameter. We apply this directly, with the same definition, to axial flux machines using the symbol α_{SR}. The airgap surface area and the average machine radius of the axial flux geometry are then expressed as functions of split ratio as given in (3.8) and (3.9) respectively.

$$A_g = \pi r_o^2(1 - \alpha_{SR}^2) \tag{3.8}$$

$$r_{av} = \frac{r_o}{2}(1 + \alpha_{SR}) \tag{3.9}$$

And finally, the torque expression is rewritten as

$$\tau = \frac{\pi \sigma_{av} r_o^3}{2}(1 + \alpha_{SR})(1 - \alpha_{SR}^2) \tag{3.10}$$

If the total axial length of the machine is l_a, the torque density (*TD*) of the machine is given in (3.11) where the total volume calculation neglects the impact of the winding end-turns.

$$TD = \frac{\tau}{\pi r_o^2 l_a} = \frac{\sigma_{av} r_o (1 + \alpha_{SR})(1 - \alpha_{SR}^2)}{2 l_a} \tag{3.11}$$

Now we explore the two previously described ways of doubling the airgap surface area and the effects these changes have on the torque density of the machine. In the first case, another stator is added on the opposite side of the rotor, creating a second airgap; thus, the total required magnet thickness also doubles in order to maintain the same magnetic loading (see Eq. 3.1). Because the electrical loading is also kept constant, the geometry of each stator remains unchanged from the original single-sided baseline version (see Eq. 3.7). This new machine has twice the airgap area of the single sided machine at the same torque radius, so the torque doubles. The total axial length does not quite double since the rotor iron has become unnecessary. However, the focus of this study is on machines with high pole counts, where the necessary rotor iron thickness tends to zero as the pole count rises (Fig. 3.6); so we assume a doubling of the axial length in order to simplify the analysis. Thus, the total machine volume doubles and the torque density remains the same as in the original single-sided machine.

In the second case, the new outer radius, r_o', of the single-sided machine that is required to double the original airgap area can be calculated from simple geometry as

$$r_o' = \sqrt{2} r_o \tag{3.12}$$

assuming that α_{SR} is unchanged. The torque output, τ', of this larger machine is then

$$\tau' = \sigma_{av}(2A_g)(\sqrt{2}r_o) = 2\sqrt{2}\tau \tag{3.13}$$

Since both the magnetic and electric loadings are kept constant, the magnet thickness and stator axial length are unchanged. So it is a reasonable assumption that the volume of this machine doubles as the airgap surface area is doubled. It should be noted that more stator yoke and rotor back-iron would be needed at the same pole count (Fig. 3.6); however, a good designer would increase the pole count for the larger diameter to better handle end turn wastage. The torque density of this larger, single-sided machine is then

$$TD' = \frac{\tau'}{V'} = \frac{2\sqrt{2}\tau}{2V} = \sqrt{2}TD \tag{3.14}$$

This analysis has shown that while doubling the amount of active material in a single-sided axial flux PM machine at the same radius to produce a double-sided machine results in the same torque density (as the original version), reallocating that extra material to a larger single-sided machine results in an increase in torque density by a factor of 1.414. Therefore, it is concluded that a single-sided machine has a torque density that is ~41% higher than that of a double-sided machine.

3.3 Axial Flux versus Radial Flux Machines

The difficulty in making comparisons between machine geometries is bound up in the issue of attempting to compare apples with apples. Various constraints are imposed by researches to try and force equality in comparison; the end result is often that the constraints themselves favor one geometry over another, leading to inconclusive results. The two aspects of AF and RF machines that will be discussed here are the rotor volume and airgap surface area advantages enjoyed by the AF structure when compared to the traditional inner-rotor RF geometry. The imposed constraints are clearly outlined and it is the authors aim to identify any biases introduced by said constraints.

3.3.1 Optimal Split Ratio

The metrics used in the ensuing comparison between radial and axial flux machine structures are the torque density, or torque per unit of total volume needed to house the active materials and the specific torque, or torque per unit mass of the active materials. The torque density of a radial-flux machine is written as a function of split ratio as

$$TD = \frac{\sigma(2\pi\alpha_{SR}r_o l_a)(\alpha_{SR}r_o)}{\pi r_o^2 l_a} = 2\sigma\alpha_{SR}^2 \tag{3.15}$$

However, this expression does not fully define the dependency of torque density on split ratio because electric loading (and hence the airgap shear stress) can also be expanded as a function of split ratio. The optimum split ratio, in terms of torque density, for a radial flux machine is presented by Pang, et al. (2006) as a function of both the number of slots in the machine and the ratio of magnetic loading (B_m) to the maximum steel flux density (B_t). The derivation is based on general purpose sizing equations and while the mathematics will not be repeated here, plots are included in Fig. 3.5 to show the optimal split ratio for a radial flux machine as it varies with the slot count and the flux density ratio, B_m/B_t (Pang, 2006).

In terms of maximum torque production for a fixed outer diameter in an axial flux machine, the optimal split ratio has been shown to be α_{SR} = 0.577 (Simsir, 1999) (Spooner, 1992). Additionally, it is apparent that as the split ratio increases closer to unity and the outer machine radius approaches infinity, the specific torque of the machine improves; however, this is an impractical result because it implies a machine with zero mass and infinite diameter. As a point of practicality, split ratio values between 0.577 and 0.650 are considered to be within the optimum range for an axial flux machine (Simsir, 1999).

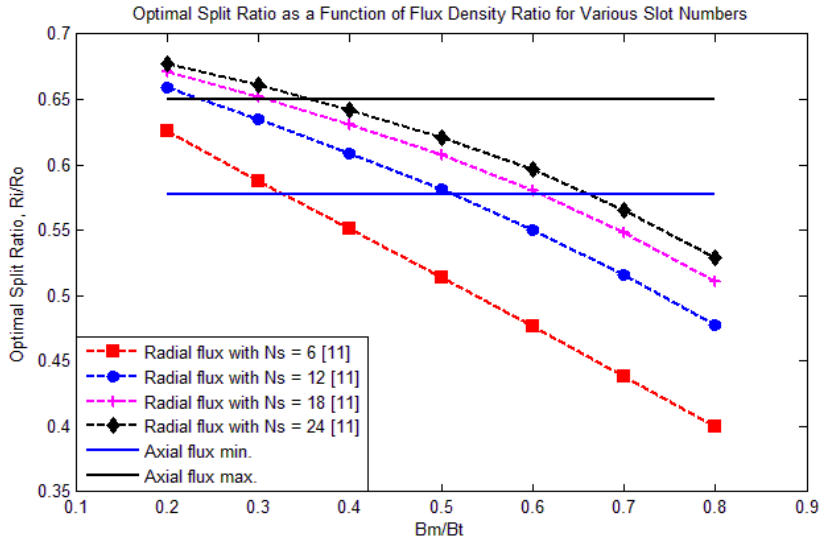

(a)

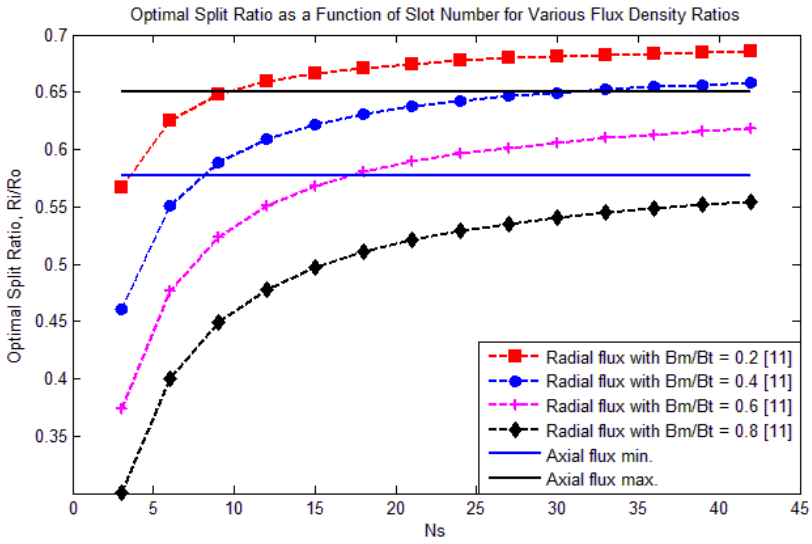

(b)

Fig. 3.5. Plots showing the optimal split ratio for a radial flux machine as determined by Pang, et al. (2006), in comparison with those of an axial flux machine. Optimal split ratio is shown as a function of (a) the number of slots in the machine and (b) the ratio of peak flux density in the airgap (B_m) to that in the steel (B_t).

3.3.2 Rotor Volumetric Advantage

There is a definite rotor volumetric advantage to axial flux machines at reasonably high pole counts. A large part of the inside volume of a traditional radial flux rotor, or indeed the stator in an outer rotor radial flux machine, is not used electromagnetically. Ingenious solutions for "slinky" style wound stators for outer rotor machines and spiders to support a rotor structure will not save on total volume, but will save active material and hence, both active and passive mass. An estimate of the volume "wasted", i.e. not used electromagnetically, will now be given for both an axial flux and radial flux rotor.

Fig. 3.6-a depicts a side view cut-away of an axial flux PM machine that has been adapted to a linear coordinate system in order to ease the ensuing geometrical descriptions. In this diagram, l_r represents the thickness of the rotor backiron that is penetrated magnetically and l_y is the thickness of the stator yoke. Note that the dimensions discussed are equally applicable to a radial flux PM machine cross-section if the label for the axial direction is replaced with the radial direction as explained in Fig. 3.6-b.

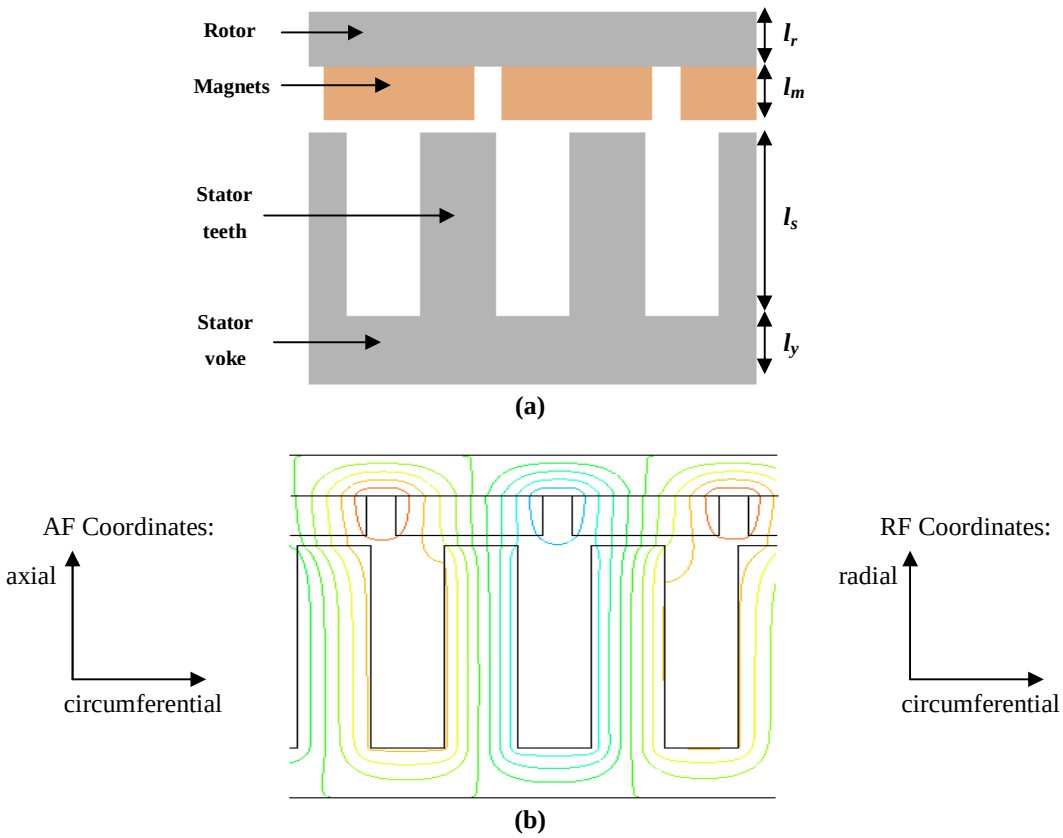

Fig. 3.6. Structure and dimensions of a surface mount PM machine are shown in (a) and (b) illustrates the PM flux paths. The representations shown are linear, but equally applicable to RF or AF structures according to the coordinate systems indicated in (b).

The axial flux structure has the advantage that the rotor thickness can be designed to be exactly as thick as is required to obtain the desired flux density in the steel (B_t). Because of this, the only wasted volume in the rotor plate is the center disk up to the stator inner radius so that the fraction of rotor volume that remains unused is simply $\alpha_{SR}{}^2$. If we assume that the axial flux machine is designed with a split ratio in the "usual" optimum range, then the fraction of rotor volume wasted is between 33% and 42% of the total rotor volume.

It should be apparent that the ratio of flux density in the airgap to that in the rotor backiron is the inverse of the ratio of the respective cross-sectional areas carrying the flux. Note that only half of the flux lines crossing the airgap and entering a tooth pass through a cross section of the rotor back-iron (Fig. 3.6-b). For the radial flux structure, this ratio can be expressed as

$$\frac{B_m}{B_t} = \frac{2 l_r l_a}{\left(\frac{\theta_m}{\theta_p}\right)\left(\frac{2\pi\alpha_{SR} r_o}{p}\right) l_a} = \frac{\theta_p}{\theta_m}\frac{l_r p}{\pi\alpha_{SR} r_o} \tag{3.16}$$

where the airgap length has been neglected. Eq. (3.16) can be used to calculate l_r for a given machine size, pole count and flux density ratio; however, unlike the axial flux design, the rotor thickness in a radial flux machine cannot be adjusted to exactly match this quantity. The fraction of rotor volume that is wasted (δ_{rad}) can then be determined by

$$\delta_{rad} = \frac{\pi(\alpha_{SR} r_o - l_m - l_r)^2 l_a}{\pi(\alpha_{SR} r_o - l_m)^2 l_a} = \left(1 - \frac{\pi \alpha_{SR} r_o}{p(\alpha_{SR} r_o - l_m)} \frac{\theta_m}{\theta_p} \frac{B_m}{B_t}\right)^2 \tag{3.17}$$

In order to quantify the rotor volume that is wasted in various radial flux machine designs, we make assumptions about some of the parameters used in (3.17):

1. The airgap thickness is fixed at l_g = 1 mm.
2. The desired magnetic loading is fixed at B_m = 0.8 T.
3. The magnets used in the design have a remnant flux density of B_r = 1 T. (Note: This is less than that of sintered NdFeB (N35) which have B_r = 1.23 T.)
4. The ratio of magnet pole arc to pole pitch is fixed at θ_m/θ_p = 0.9.

From assumptions 1-3 above, (3.1) can be used to calculate a necessary magnet thickness of l_m = 4 mm. Fig. 3.7-a shows a plot of δ_{rad} as a function of pole count and machine rotor radius ($\alpha_{SR} r_o$) at a fixed flux density ratio of B_m/B_t = 0.5 while Fig. 3.7-b shows δ_{rad} as a function of flux density ratio and machine rotor radius for a fixed pole count of p = 8. This shows that for machines with pole counts greater than six, the axial flux structure will always exhibit higher rotor volume utilization than that of a radial flux machine for any machine size.

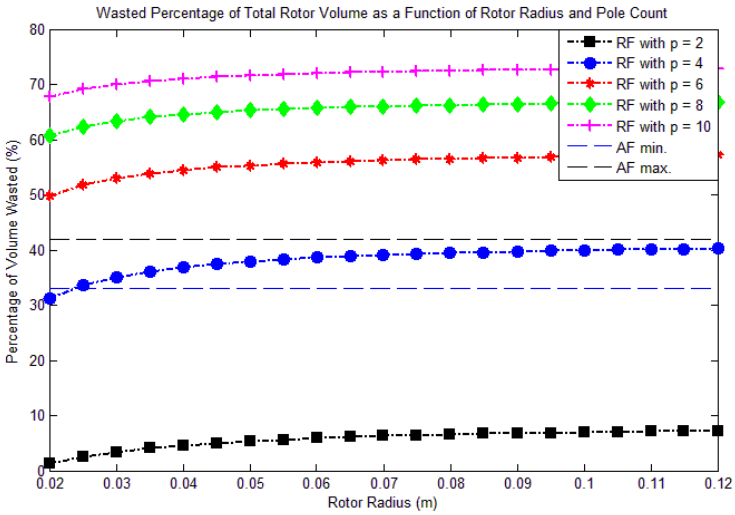

(a)

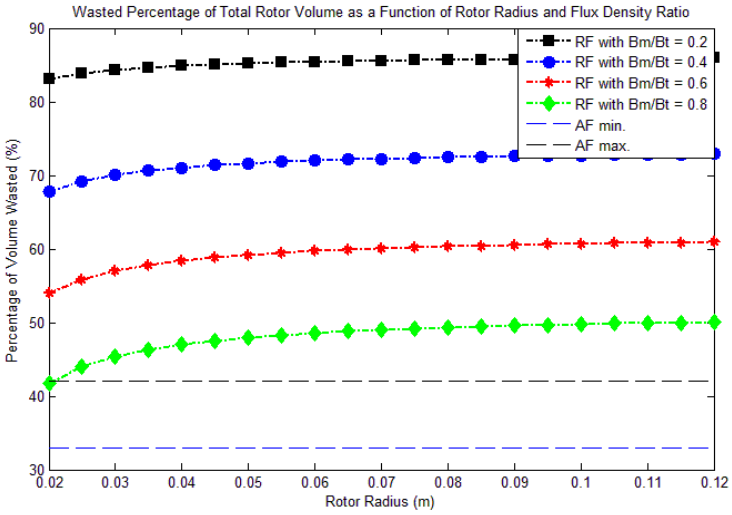

(b)

Fig. 3.7. Plot showing the percentage of back-iron volume that remains unused electromagnetically for a radial flux rotor.

3.3.3 Torque Production

In this section, it is shown that the single-sided axial flux machine typically requires a lower airgap surface area for a given torque specification and (average) shear stress design point than a traditional radial flux machine. For the axial flux geometry, (3.8) and (3.10) can be combined to yield the expression for the airgap surface area (as a function of split ratio) given by

$$A_{g\_AF} = \pi(1 - \alpha_{SR}^2)\left(\frac{2\tau}{\sigma_{av}\pi(1 + \alpha_{SR} - \alpha_{SR}^2 - \alpha_{SR}^3)}\right)^{2/3} \tag{3.18}$$

For the radial flux structure, the symbol α_{asp} is introduced to represent the aspect ratio, or rotor diameter to length ratio (r_i/l_a). Then the torque production can be expressed as

$$\tau = 4\sigma\pi r_o^3\left(\frac{\alpha_{SR}^3}{\alpha_{asp}}\right) \tag{3.19}$$

This can be solved for the machine radius and used to determine the required airgap surface area as given by

$$A_{g\_RF} = \frac{4\pi}{\alpha_{asp}} \left(\frac{\tau \alpha_{asp}}{4\pi\sigma} \right)^{2/3} \tag{3.20}$$

A torque specification of 100 Nm and an (average) electromagnetic shear stress design point of 20 kPa were used to illustrate the differences in required airgap surface areas between the axial and radial flux machine geometries as shown in Fig. 3.8. The lower area required by the single-sided axial flux machine compared with all but the most disc-like radial flux machines is significant. The cost of a PM machine is largely dominated by the amount of magnet material necessary because there is such a large difference in cost between magnets and other active materials in the machine. Since the amount of magnet material in a machine is proportional to the airgap surface area, a lower area equates to a significant reduction in cost.

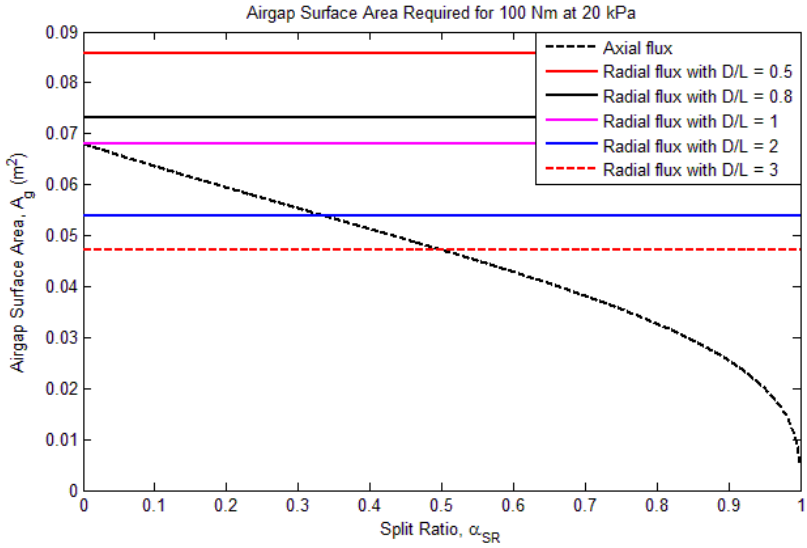

Fig. 3.8. Plot showing the required airgap surface area for an axial flux machine and radial flux machines with various aspect ratios for a torque requirement of 100 Nm and a shear stress design point of 20 kPa.

3.4 Details of Constant Electric and Magnetic Loading in Axial Flux and Radial Flux Machines

3.4.1 Magnetic Loading

One might initially expect that the cost of magnetic loading in axial and radial flux structures would be the same per unit area, but as will be discussed subsequently, this is not necessarily the case. Firstly, at this stage of axial flux technology development, it is common to use larger airgaps than are possible in a radial flux machine. This would then imply a higher cost for a given magnetic loading owing to the need for thicker magnets (Eq. 3.1). The reality is that the differences are much smaller than one might imagine and sometimes nonexistent due to the shaping of magnets required for surface mounted PMs for a radial flux machine. The necessary curved surfaces of the magnets are invariably ground to shape from a pre-sintered block of material and he cost of such magnets includes the wasted material. Thus, premiums on cost of the order of 30% are to be expected.

A second problem is the magnet retention mechanism necessary in a radial flux structure has which has several negative impacts on magnetic loading. It is common to add a glass fiber or Kevlar “bandage” around the rotor which then adds to the effective airgap from a magnetic perspective; in this way, the radial flux machine may have a larger effective airgap than an axial flux machine.

A common solution to reduce the cost of the curved magnet piece in a radial flux machine is to shallowly embed the magnets in pockets in the rotor, allowing the use of flat magnet pieces. This embedding of the magnets introduces its own repercussions on cost of magnetic loading because it provides flux shorting paths which can reduce the effective flux of the magnet by a factor of up to 20%. Furthermore, attempting to reduce the flux shorting effect must be carefully balanced against a reduced burst strength capability in over-speed conditions. A final consideration for this rotor assembly is that the manufacturing process involved can be quite challenging and ultimately add to the cost.

Thus qualitatively, we may conclude that the costs for magnetic loading are similar in both axial and radial flux machine structures. However, we have not been able to derive a generalized, workable analytic relationship so each case should be considered independently.

3.4.2 Electric Loading

The physical amount of copper contained in a slot is clearly the same for a given current density, fill factor and electric loading. Differences then appear in the end-winding wastage. However, most new machines are constructed with non-overlapped windings so the effect is less apparent

than when a traditional distributed winding scheme is used. We therefore assume that there is no significant difference in the copper cost per unit area for a given electric loading.

The stator steel is a different matter. The amount of iron necessary firstly to provide the teeth to enclose and support the copper and secondly to provide the yoke, can be computed as an area per unit length of circumference of the airgap in a radial flux machine and of the average radius in an axial flux machine. Note that these are the same lengths used in the definition for electric loading for the radial and axial flux geometries respectively. This area per length then represents the steel volume per unit stack length in a radial flux machine and per unit length of the radial stator thickness in a single-sided axial flux machine.

Unlike an axial flux machine, the slots in a radial flux machine fan out and so the width (in a circumferential direction) is a function of radius. If we consider a 2D cross-section of a radial flux machine, the total surface area allotted to slots (A_s) per unit airgap circumference can be written as

$$\frac{A_{s\_RF}}{2\pi r_i} = \frac{\left(1 - \frac{\theta_m}{\theta_p}\frac{B_m}{B_t}\right)\pi\left(\left(r_i + l_{s,RF}\right)^2 - r_i^2\right)}{2\pi r_i} \tag{3.21}$$

where again, the airgap thickness is neglected. Similarly for the axial flux structure, the total slot cross-sectional area per unit circumferential length at the average radius is given by

$$\frac{A_{s\_AF}}{2\pi r_{av}} = \left(1 - \frac{\theta_m}{\theta_p}\frac{B_m}{B_t}\right) l_{s,AF} \tag{3.22}$$

In order to constrain the copper cost to be the same for a given electric loading in each machine geometry, we equate (3.21) and (3.22) to obtain an quadratic equation in $l_{s,RF}$. Taking only the positive root, an expression for $l_{s,RF}$ can is determined as a function of $l_{s,AF}$ to be

$$l_{s,RF} = r_i\left(-1 + \sqrt{1 + \frac{2l_{s,AF}}{r_i}}\right) \tag{3.23}$$

The yoke thickness, l_y, which is assumed to be constant from the bottom of the stator slot to the outer radius in the radial flux geometry or the back of the stator in the axial flux structure, can be determined using the same logic as was used in section 3.3.2 to ascertain the necessary rotor thickness. The expression for the axial flux machine is

$$l_y = \frac{\pi r_{av}}{N_s}\frac{\theta_m}{\theta_p}\frac{B_m}{B_t} \tag{3.24}$$

and the radial flux geometrical calculations result in the same equation with r_{av} replaced with r_i. We make the simplifying assumption that $r_{av} = r_i$.

Given these, the surface area of the annulus needed for the radial flux machine per unit circumferential length, ignoring the scrap cut out for slots can be readily computed from knowledge of $l_{s,RF}$ and l_y. The axial case is similarly simple. For comparative purposes, Fig. 3.9 shows, for r_i = 50 mm and a range of axial slot lengths from 2 to 30 mm, the fractional increase in steel required for constant electric loading in a radial flux machine when compared to an axial flux machine.

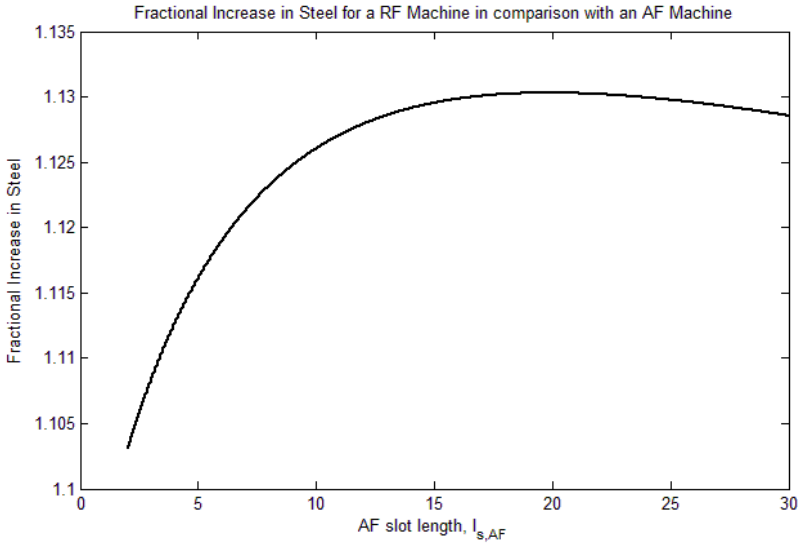

Fig. 3.9. The fractional increase in steel, in a RF machine when compared with an AF machine, necessary to provide the same electric loading. The results shown are for r_i = 50 mm, N_s = 9 and $l_{s,AF}$ is allowed to vary.

3.5 Auxiliary Issues

The observation presented in the introduction regarding the relative uptake of the single-sided axial flux PM machine both in academia and industry is revealing. There is a range of issues, some of which are reputed to rule out the axial flux structure as a viable solution and others of which are claimed to be significant advantages. Of course some of these issues have more basis in scientific fact than others and the purpose of this section is to introduce a sampling of these.

1. **Axial Attractive Force**

   This is high in single-sided axial flux machines and is usually a surprise to most people when they first encounter it which leads to concerns. However, standard deep-groove ball bearings do have quite a high axial load rating and careful design and testing has shown that standard ball bearings, when correctly used and sized, are entirely adequate in a well-designed machine. In fact, it is common practice to add axial loads to radial flux machines using wave washers in order to reduce bearing noise during operation. Fasco Australia has recently taken out a patent for a method of reversing the usual wave washer thrust on one of the machine bearings with the purpose of reducing the net magnetic force (Langford, 2010).

2. **Stator Construction**

   Prototypes and small production quantities of single-sided axial flux machines are invariably produced by the expensive process of milling or spark eroding slots in a tape-wound toroid. However, mechanically controlled “punch and wind” machines abound in the patent literature and a lesser number of successful machines have been in operation for many years. Fasco Australia has developed a numerically controlled machine with a single punch and die that produces stators at a high rate with low cost (Patterson, 2010). The advantages of the method are that the slot shape can be easily changed and the only steel wasted in the process is that cut out for the slots. Such a stator production method should be rigorously compared to the very expensive progressive die machines used for large-scale radial flux machine stator lamination production.

3. **Stator Coils**

   With the assumption that the machine design is done with open stator slots and a non-overlapped winding scheme in which a coil spans a single tooth, the coils in an axial flux machine are planar (regardless of whether the machine is single- or double-sided). Thus they are very easy to wind and place and the use of rectangular section copper for high

performance machines is comparatively simpler when compared with the process of winding coils for radial flux machines.

4. **Airgap Maintenance**

   The axial flux geometry does not lend itself well to the small airgaps traditionally required in machines, prior to common use of rare earth magnet materials for field generation. However, the discussion presented in this paper is regarding PM machines which allow the machine designer to impose a larger airgap while still achieving good performance. That said, the efforts of practicing engineers in the process of continuous improvement is a remarkable thing and we are thence finding ways to gradually refine our airgap tolerances and reduce the airgap length.

5. **Magnet Retention**

   This is a substantial positive attribute of the axial flux geometry, either single- or double-sided, where a simple lip on the rotor can manage magnet retention with no practical speed limitation. Additionally, the magnet retention mechanism on an axial flux machine is external to the main flux paths so as not to interfere with operational characteristics.

6. **Heat Paths**

   In many applications, it is relatively easy to allow the rotor of a single-sided axial flux PM machine to enjoy very poor heat paths from the primary source of heat in the stator even for an air-cooled machine. This protects the heat-sensitive rare earth permanent magnets and allows for a lower heat specification for the magnet material, thereby mitigating some costs. Furthermore, the flat back of the stator may be arranged to have excellent heat paths to its mounting surface.

Chapter 4

Design of the Integrated Starter-Alternator

The fact that the application for this machine is an integrated starter-alternator (ISA) for a series hybrid electric vehicle (HEV) greatly simplifies the design process because the machine can be optimally designed around a single torque-speed operating point instead of over a range of values. This machine will operate predominantly in generating mode, but it must also be capable of motoring operation to supply the required starting torque of the internal combustion engine (ICE) up to a given speed. So generally speaking, the design challenge inherent to this type of application is that the torque requirement of the machine during motoring is often much larger than the nominal operating torque when the machine is in generation mode. In this chapter, the performance criteria for the machine are quantified based on characterization of both the ICE and the energy storage system of the vehicle and a full account of the design process is detailed, including justification of all design choices.

4.1 Specification of the Performance Criteria

An investigation of the relevant characteristics of the vehicle's energy storage system and the ICE chosen for this application will now be presented. The goal is to determine the torque-speed

operating point and any electrical characteristics around which the integrated starter-alternator should be designed.

4.1.1 The Internal Combustion Engine

The primary advantage of a series-HEV in comparison to a parallel-HEV is the disconnection of the ICE from the driveline of the vehicle. This not only permits the utilization of a smaller capacity ICE, but also ensures that the operating conditions of the engine are independent of the driving demands on the vehicle. The objective of the ICE testing procedure is to specify a single torque-speed operating point of the engine that corresponds to its maximum fuel efficiency since it is assumed that the engine will be run only at this operating point or not at all. The design of the ISA will then be based around this particular torque-speed condition.

The model of engine chosen for this project is a Honda GX390 engine with datasheet parameters as listed below in Fig. 4.1. The primary characteristics of interest are the maximum output power of 8.7 kW and peak torque output of 26.4 Nm, although the actual output of the engine depends on a number of factors including the operating speed of the engine (Fig. 4.1). In order to determine the peak fuel efficiency of the engine, a measure of brake specific fuel consumption (BSFC), defined as the ratio of the rate of fuel consumption to shaft output power, is taken at a variety of loads and engine speeds as shown in Fig. 4.2. The testing of the ICE was performed at the University of Nebraska Tractor Test Laboratory using a SuperFlow engine dynamometer setup.

Specification	Description
Engine type	4-stroke, overhead valve, single cylinder
Dimensions (L x W x H)	407 x 459 x 449 mm
Dry weight	31.5 kg
Peak power	**8.7 kW (at 3600 rpm)**
Peak torque	**26.4 Nm (at 2500 rpm)**
Displacement	389 cm^3
Bore x Stroke	88 x 64 mm
Compression Ratio	8.2 : 1
Lubrication system	Splash

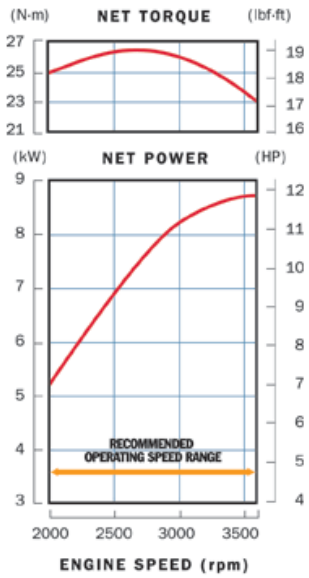

Fig. 4.1. Datasheet specifications for the Honda GX390 engine.

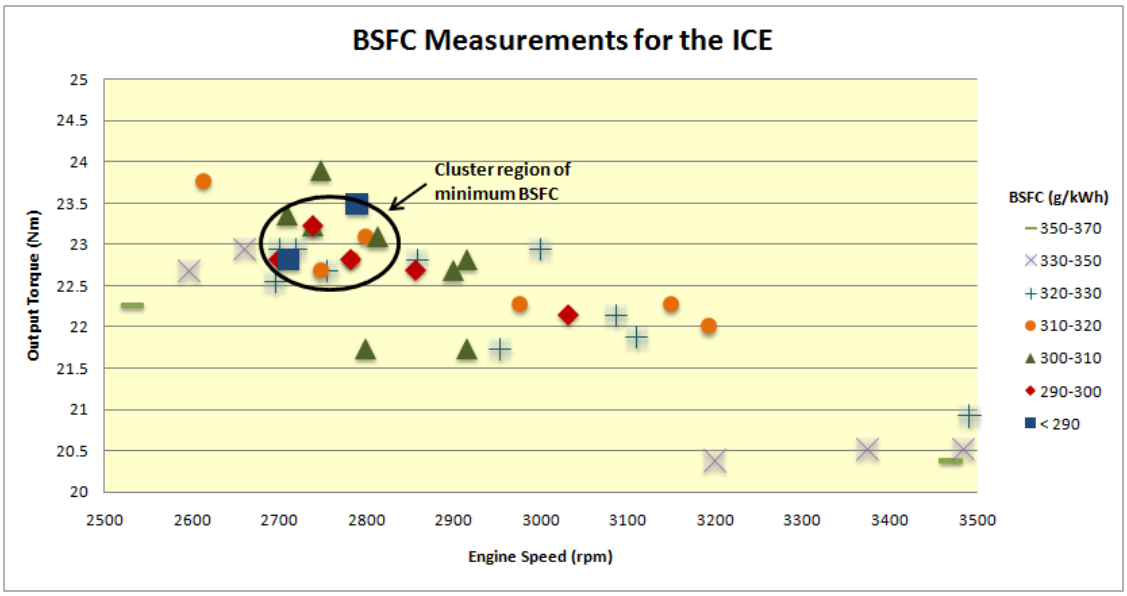

Fig. 4.2. BSFC map of the ICE for a range of torque-speed operating points. Note that peak fuel efficiency of the ICE is indicated by minimum BSFC.

From these measurements, it can be seen that the high fuel efficiency (low BSFC) operating points are clustered around engine speeds between 2700 and 2800 rpm for torque outputs ranging from 22.5 to 23.5 Nm. The irregularity in the sample points shown in Fig. 4.2 is indicative of the difficulties encountered in stabilizing the ICE at a single operating point for any length of time. Further testing in order to corroborate the results shown was unable to be performed due to limitations in access to the appropriate facilities. Regardless of these issues, it is determined that the generation mode design parameters of the integrated starter-alternator (ISA) will be based around the nominal operating point of 23 Nm at 2800 rpm, corresponding to a power output of 6.7 kW.

4.1.2 Electrical Requirements

The ISA will be interfaced to the energy storage system of the vehicle via a three-phase converter that allows bidirectional power flow, thereby performing inverter functions during motoring mode and rectification for generation mode operation (see Fig. 1.1). The design of this converter block is beyond the scope of this dissertation; however, for machine design purposes, it is assumed that it consists of a three-phase rectifier/inverter on the machine side coupled with a DC-DC converter on the battery side as shown in Fig. 4.3. In order to not only keep the components

of the converter small but also to minimize losses in the converter, it is desirable for the rectified voltage output of the generator to be roughly equal to the desired battery bus voltage. The battery bank for the vehicle consists of 64 cells, each at a nominal voltage of 3.7 V (peak of 4.2V), connected in series to give a nominal bus voltage of 236.8 V. The RMS value of the output of the six-pulse rectifier is equal to 1.655 times the peak value of the phase voltage. Therefore the machine will be designed to have a per-phase peak output voltage of approximately 143 V at the nominal speed of 2800 rpm, corresponding to a per-phase machine constant of 0.488 $V_{pk,l\text{-}n}$/(rad/s).

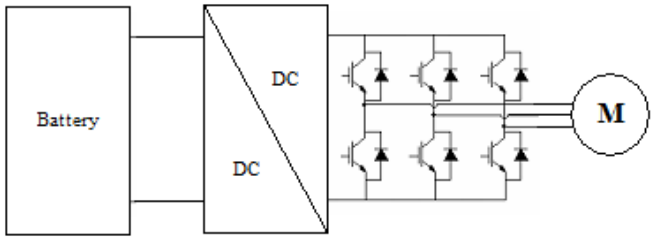

Fig. 4.3. Block diagram of the power electronics system connecting the ISA with the battery bank.

4.2 Stator Design

The machine geometry chosen for this application is a single-sided AF PM machine, as discussed previously, so this section will include details about the single stator.

4.2.1 Machine Sizing

In sizing this particular machine, we work around the torque specification discussed in section 4.1 where all dimensions of the machine are essentially free. Eq. (3.10) gives the expression for torque in an AF machine as a function of outer radius and split ratio (α_{SR}). The concept of optimal split ratio for AF machines, as discussed in section 3.3.1, is a topic of current research. In order to illustrate what happens to the machine design with variation of the split ratio, we begin by specifying a nominal torque of between 22.8 and 23.2 Nm and then compute combinations of inner and outer radii, using (3.10) with σ_{AV} = 15 kPa. The following constraints are imposed on all the designs being analyzed.

1. Equal electric (A_e) and magnetic (B_m) loadings.
2. Equal current densities (J).

3. Equal peak steel flux density (B_t).
4. Equal magnet pole arc to pole pitch ratios (θ_m/θ_p).
5. Fixed number of slots per meter as at the average machine radius (Q).
6. Fixed number of poles per meter at the average machine radius (P).
7. Equal airgap thickness (l_g) and magnet remnant flux density (B_r).

Three metrics of comparison were used to evaluate the designs: (1) specific torque (Nm/kg) or torque per unit mass of active materials, (2) torque density (Nm/m^3) or torque per unit volume of the total package, including the added volume resulting from the winding end-turns and (3) cost per unit torque ($/Nm) of the active materials. The windings are assumed to be of the DL NOW variety. Fig. 4.4 shows the specific torque and torque density as a function of split ratio for the parameter values as listed in Table 4.1, while the cost trend for the designs is indicated in Fig. 4.5. Machines with split ratio values less than approximately α_{SR} = 0.45 are not included in the analysis because the slot width necessary to maintain B_m/B_t = 0.5 resulted in a tooth width that was at or below zero at the inner machine radius. Fig. 4.6 does show the continuation of the specific torque and torque density trends for split ratios between 0.2 and 1 by increasing B_m/B_t to 0.9 (indicating a lower design point for the flux density level in the steel). In reality however, there does exist a minimum value for the inner machine radius as it is necessary to accommodate the inner winding end-turns as well as the rotor shaft. The details of the calculations used in deriving these results can be found in Appendix A.

From these trends, it is obvious that the torque density and specific torque cannot generally be maximized simultaneously, so selection of the optimal split ratio depends on the relative importance of these two concepts. The dollar cost trend indicates an optimal split ratio closer to α_{SR} = 1. This is because the cost of magnet material (NdFeB is considered here) is much higher than that for the steel and copper, so the minimum total cost for the machine occurs for the designs with the lowest airgap surface areas. The relative cost function for this application is someone arbitrary, so a split ratio target of α_{SR} = 0.6 was selected. The machine sizing was completed for a shear stress of 15 kPa and all pertinent parameters as listed in Table 4.1, resulting in machine dimensions of r_o = 98 mm and r_i = 58 mm.

TABLE 4.1 Parameter Values Used to Evaluate Machine Designs with Varying Split Ratio

Parameter	Value		Parameter	Value
θ_m/θ_t	0.75		Q (m^{-1})	60
B_m (T)	0.8		P (m^{-1})	40
B_m/B_t	0.5		B_r (T)	1.0
J (A/m^2)	2.0×10^6		l_g (m)	0.001

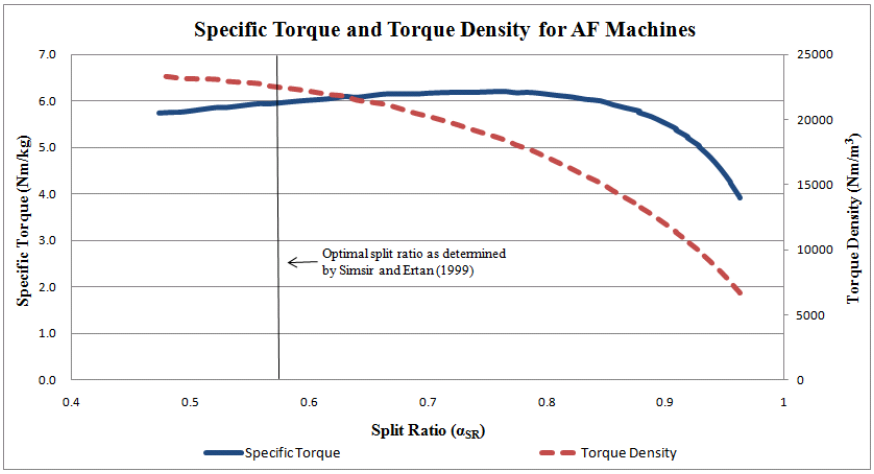

Fig. 4.4 Torque density and specific torque as a function of split ratio in AF machines with parameter values as given in Table 1.

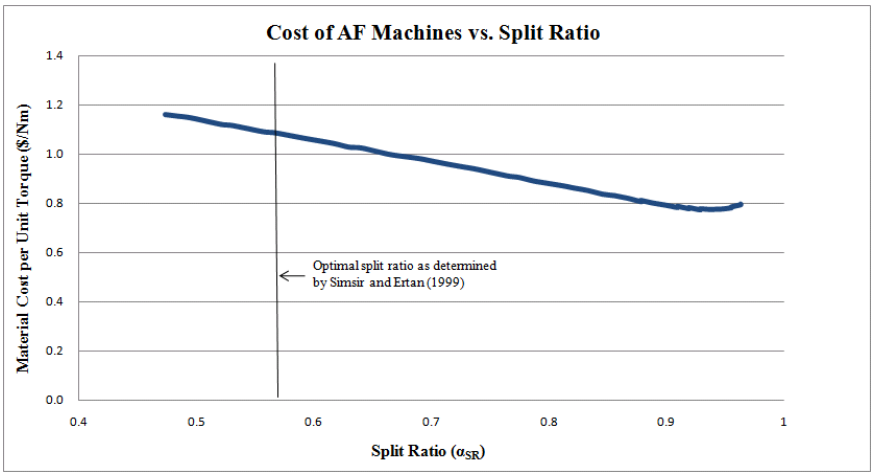

Fig. 4.5 Cost per unit torque as a function of split ratio in AF machines with parameter values as given in Table 1.

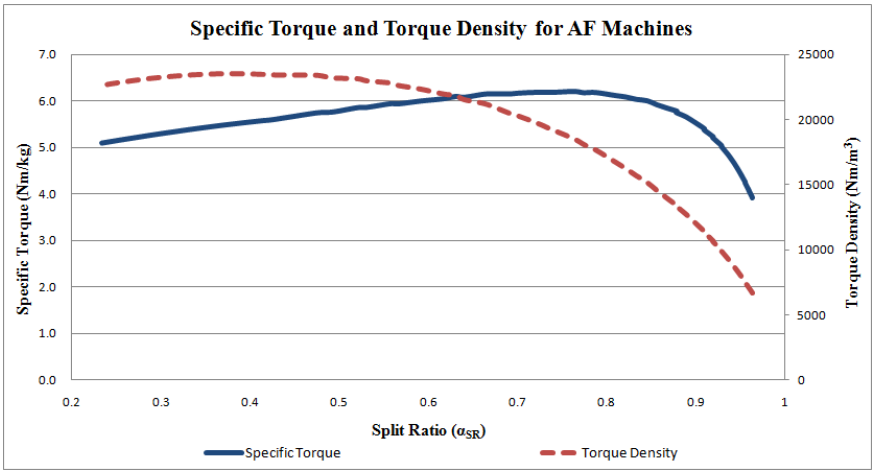

Fig. 4.6 Torque density and specific torque as a function of split ratio in AF machines with parameter values as given in Table 1 except that here $B_m/B_t = 0.9$.

4.2.2 Selection of Slot and Pole Counts

As discussed previously, this winding configuration chosen for this machine will be of the NOW variety. The particular slot and pole counts selected for this application have impacts on several aspects of the machine performance and so important areas of consideration are: (1) rotor losses, (2) main harmonic winding factors and (3) practical concerns such as physical construction and electrical frequency limitations. It is important to note that the machine to be constructed for this application is intended as a proof-of-concept and so design choices that are described here may differ in a setting where many thousands of machines will be produced on an assembly line.

It is assumed that a high-performance sinusoidal drive will be used to control this machine and as such, even with state-of-the-art power electronics techniques, there is an upper limit to the frequency that can be achieved by the drive. The nominal speed of this machine is 2800 rpm (section 4.1.1); however, it is only necessary for the drive to supply the machine in motoring mode, in order to start the ICE, up to a much lower speed. The drive accessible in this laboratory is a 20-HP DURApulse (model GS3-2020), which has a maximum frequency for sinusoidal drive of 400 Hz. If we take a conservative design approach, and assume that the drive must supply the machine up to a base speed of 2000 rpm, the pole count for this application is then limited to 24 poles. It is advantageous, in terms of rotor design and end-winding management to select a high pole count, so only machines with $p = 20$, 22 or 24 were seriously considered for implementation. According to (Cros 2002), a NOW configuration for a three-phase machine is possible when the constraint

$$\frac{N_s}{3 \cdot GCD\{N_s, {}^{p}/_{2}\}} = integer \tag{4.1}$$

is adhered to. Table 4.2 shows the slot and pole combinations that are feasible for this application.

TABLE 4.2 Slot and Pole Combinations Considered for the ISA Design

Poles (p)	**Slots (N_s)**
24	45, **36**, 27, **18**
22	45, **42**, 39, **36**, 33, **30**, 27, **24**, 21, **18**, 15, **12**
20	45, **42**, 39, **36**, 33, 27, **24**, 21, **18**, 15, **12**

It was decided that two prototype machines would be constructed with the same slot and pole count, but one should have a DL winding and the other a SL winding. In this way, it is possible to investigate the differences in machine performance between the two schemes. In order for a SL winding to be possible, two conditions must be met (Bianchi, 2007):

1. N_s must be even, AND
2. Either $GCD\{N_s, p/2\}$ must be even or $\frac{N_s}{GCD\{N_s, p/2\}}$ must be even.

The machines with slot numbers that lend themselves to a SL NOW are indicated in Table 4.2, highlighted in red. The winding factors for the main (torque-producing) harmonic for each slot-pole combination are calculated as in (Bianchi, 2007) and are shown in Table 4.3, below. Note that the winding factor for a SL winding is always greater than or equal to that of its DL counterpart (Bianchi, 2007). The highest winding factors occur for machines with slot counts of 24 or 42 corresponding to either 22 or 20 poles.

In terms of rotor losses for NOW machines, it was determined by Bianchi et al. (2010) that local minima occur for the relation $N_s/p = 1.5$ for both SL and DL schemes, in addition to $N_s = p$ for SL machines and $N_s/p = 2.5$ for the DL case. The 24 slot, 22 pole combination comes closest to the minimum for the SL winding, so that is the slot-pole combination selected for this application.

TABLE 4.3 Winding Factors of the Main Harmonic for Various Slot-Pole Combinations

N_s / p	**42**	**36**	**30**	**24**	**18**	**12**
24	-	0.866	-	-	0.866	-
22	0.953	0.902 SL 0.899 DL	0.875	0.957 SL 0.949 DL	0.902	0.259 SL 0.250 DL
20	0.953	0.946	-	0.966 SL 0.933 DL	0.946	0.250

4.2.3 Slot and Winding Design

The necessary width (w_s) and depth (l_s) of the stator slots can be determined by (3.6) and (3.7) respectively, with the following parameter values:

1. The magnet pole arc to pole pitch ratio is assumed to be $\theta_m/\theta_p = 1$. The actual value of this is designed as described in section 4.3.
2. The ratio of magnetic loading to steel flux density is $B_m/B_t = 0.64$. The magnetic loading is 0.8 T and the target steel flux density is conservative at 1.25 T in order to better manage the stator core losses.
3. The electric loading at the average radius is A_e = 18,750 A/m. This comes from (3.3) with a shear stress of 15 kPa and a magnetic loading of 0.8 T, where the coefficient, k, is unity to obtain the minimum electric loading.
4. The current density is $J = 1.8 \times 10^6$ A/m^2. This comes from a standard current density of 4.5 A/mm^2 and taking into account a 40% copper fill-factor (due to hand-winding).

The calculations result in w_s = 8 mm and l_s = 29 mm. However, due to several factors, including an attempt to relieve eddy-current loss in the copper windings, the actual slot depth is set at 35 mm so that the windings can be set back somewhat away from the magnets.

The stator yoke thickness that is required for electromagnetic purposes can be determined from the same logic that the rotor thickness is calculated, as

$$l_y = \frac{\theta_m}{\theta_p}\frac{B_m}{B_t}\frac{\pi r_{av}}{p} \tag{4.2}$$

For this design, the resulting yoke thickness is l_y = 7 mm. The stator yoke has the secondary functionality of providing mechanical stiffness to the machine, so this value was increased to l_y = 10 mm in the actual design.

The single-sided AF machine was modeled in 2D FEA software as described previously in section 2.1. In order to determine the number of turns per winding that is required to obtain the aforementioned per-phase machine constant of 0.488 $V_{pk,l\text{-}n}$/(rad/s), it is necessary to look at the back EMF waveform of a single phase. In order to do so, we simply apply a DC current in one phase winding (with the other phases set to zero current) and obtain the resulting torque output as the rotor is rotated over at least a full pole-pitch. This is obviously a torque waveform, not a voltage waveform; however it does contain the information of interest regarding the machine constant. The resulting torque waveform for this 24-slot/22-pole machine, with a DC current in a single phase, for a rotor rotation over exactly one pole pitch is shown in Fig. 4.7 for both the DL and SL cases. The peak torque output for the DL is approximately 7.1 Nm with 100 A-DC and so a machine constant for a single turn is calculated as 0.047 Nm/A (or equivalently V/(rad/s)). So in order to achieve 0.488 V/(rad/s), it is necessary to include approximately 10 turns per coil. As expected for the SL winding, the same peak torque output, but with 300 A-DC, suggests a requirement of 20 turns per coil; the SL winding has twice as many turns per coil, but half as many coils so that the number of turns per phase is equal to the DL case.

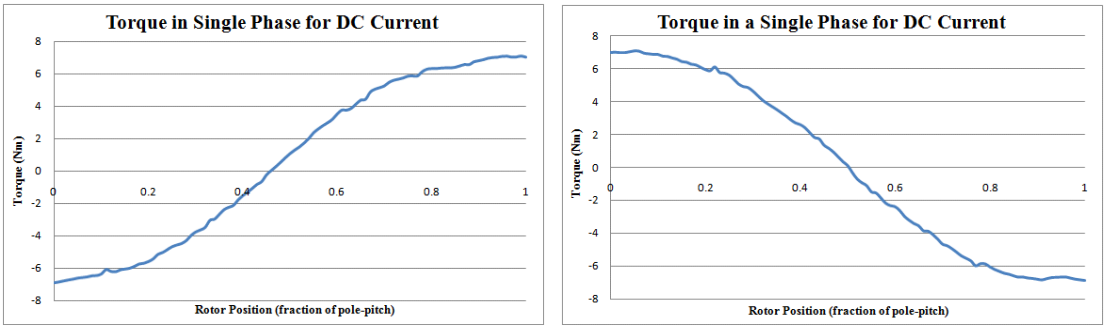

(a) **(b)**

Fig. 4.7 Torque waveform resulting when a single phase is driven with 100 A (DC) and the rotor is rotated over a single pole pitch. Currents in the two remaining phases are maintained at zero. The DL winding output is shown in (a) and that of the SL winding is indicated in (b).

With an axial slot depth of l_s = 35 mm and a slot width of w_s = 8 mm, and taking into account the 40% fill factor, this gives a total copper fill area of 112 mm^2 or 5.6 mm^2 per turn for both the SL and DL windings. This corresponds to round copper wire with a diameter of 2.7 mm (or size 10

AWG wire), which was deemed too heavy to work with by-hand. Instead, the windings were completed with 4 strands of size 16 AWG (diameter of 1.29 mm) in-hand. 2D FEA was used again in order to determine the current required to maintain a full-load average torque output of 23 Nm. The torque curves in Fig. 4.8 are shown for a total slot current of 445 Arms to get an average torque of 22.9 Nm for both winding schemes. Note that the machine with the DL winding requires a slightly larger slot current (448 Arms) to obtain the same torque output, resulting from the lower winding factor as shown in Table 4.3. With 20 turns per slot, this gives a per-phase RMS current of 22.3 A; since each turn is constructed with 4 strands of 16 AWG, the per-strand current density is ~4.3 A/mm^2, which is very conservative for a machine of this size with no forced cooling.

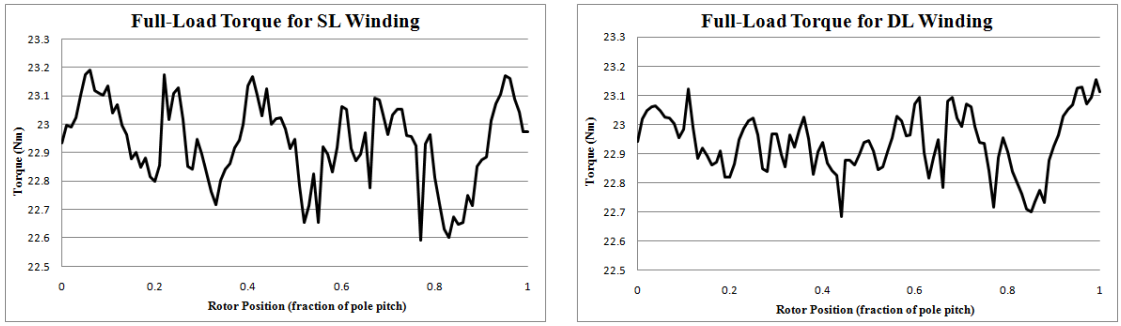

(a) **(b)**

Fig. 4.8 Full-load torque waveforms obtained via 2D FEA for (a) the SL winding and (b) the DL case.

4.3 Rotor Design

The purpose of this section is to detail the design of the rotor backiron in addition to the magnet dimensions. The rotor thickness required for electromagnetic purposes, as discussed in section 3.3.2, is given by the equation

$$l_r = \frac{\pi r_{av}}{p}\frac{\theta_m}{\theta_p}\frac{B_m}{B_t} \tag{4.3}$$

where in this design, there are 22 poles and because the rotor iron does not see the full flux reversals that the stator iron sees, the allowable steel flux density is increased to B_t = 1.6 T. The calculation results in a necessary rotor thickness of 5.6 mm, although this was rounded up to an even 6 mm for production. The necessary magnet thickness is determined from (3.1) to be l_m = 4 mm, with a desired magnetic loading of B_m = 0.8 T, a nominal airgap thickness of l_g = 1 mm and

a remanent flux density of B_r = 1 T. Actually, sintered NdFeB (N35) magnets, which have B_r = 1.23 T will be used in this machine, however the lower flux density was used to obtain a conservative design in the event that the magnet quality is not as expected. In the physical structure of the machine, it is possible to adjust the airgap if necessary. Fig. 4.9 shows the 2D FEA verification of the no-load flux densities achieved in the machine.

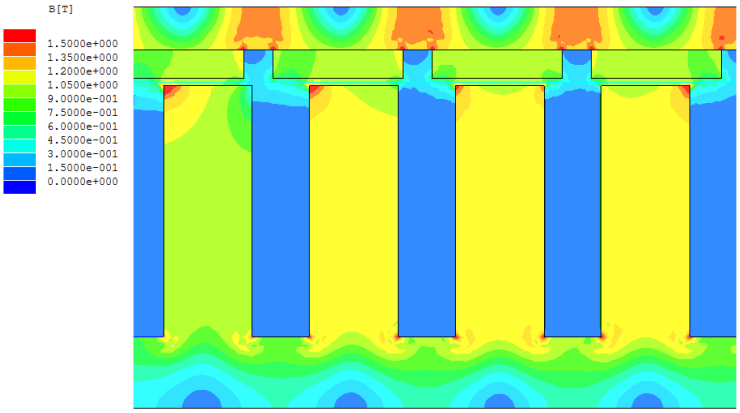

Fig. 4.9 2D FEA calculation of the no-load flux densities achieved in the machine for the described design.

As an additional requirement, the magnet thickness must be designed so as to resist demagnetization when the machine is operating at maximum load. It was not possible to measure the necessary cranking torque for the ICE used in this application, however, an assumption is made that four times the rated torque is required to start the engine. Fig. 4.10-a shows the magnet flux for full load operation for the machine with both SL and DL windings, while Figs. 4.10-b and 4.10-c show the same information for operation at 200% and 370% rated torque respectively. From this, we see that flux reversal in the magnets does not occur because the flux density in the magnets is not forced below 0.3 T. Thus, the magnet thickness of l_m = 4 mm is sufficient to resist demagnetization even in overload conditions.

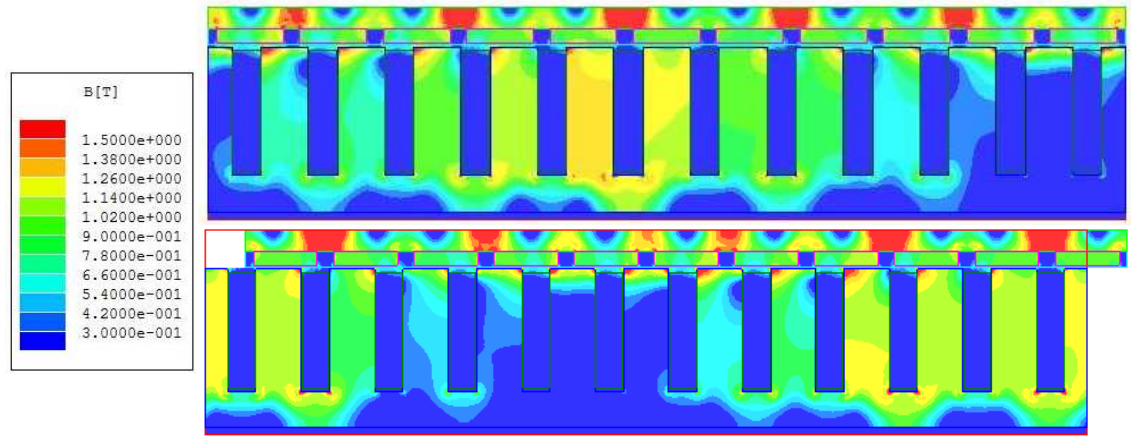

(a)

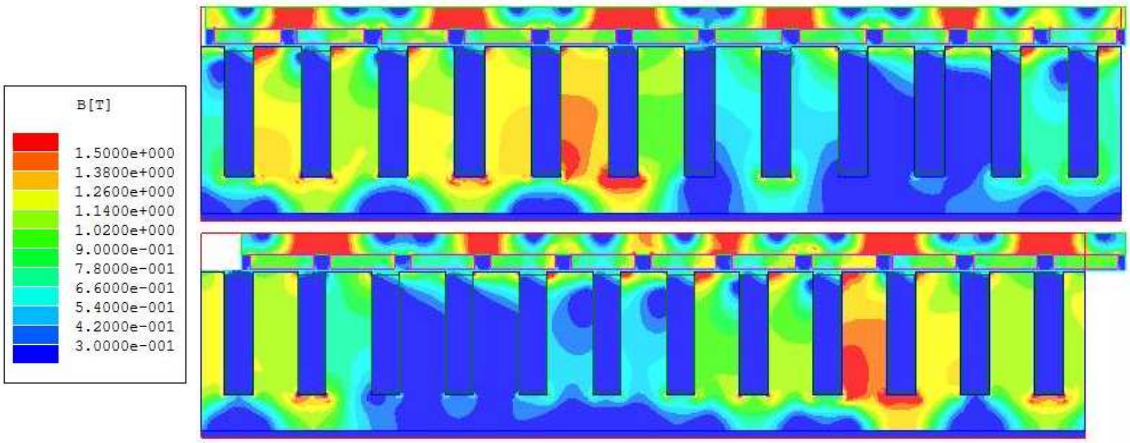

(b)

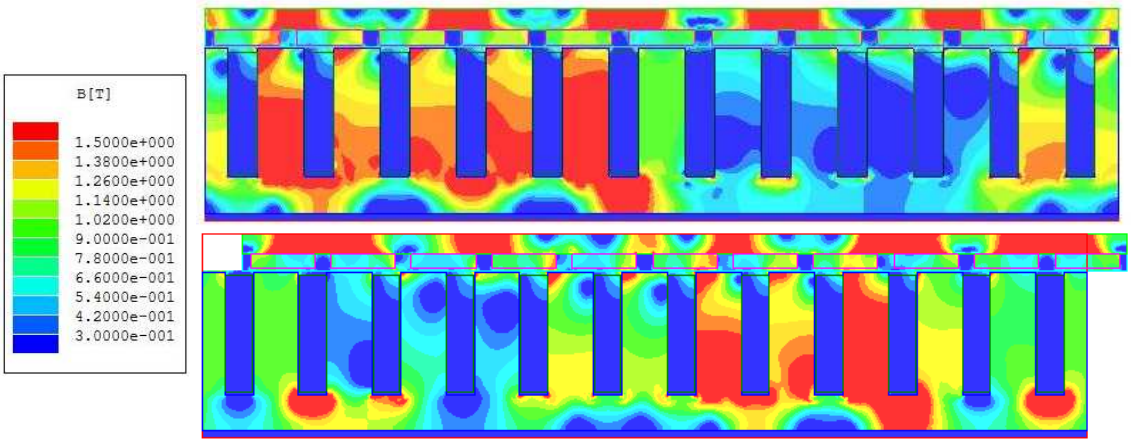

(c)

Fig. 4.10 2D FEA flux plots of the designed machine for (a) rated load, (b) 200% rated load and (c) 370% rated load for two different time instants at each loading. The flux density in the magnets is not pushed below 0.3 T even under overload conditions.

A machine designed with NOW inherently presents a lower cogging torque in comparison with a machine with a traditional winding scheme (Aydin, 2007). This happens because the cogging component associated with an individual magnet is out of phase with those of the other magnets and thus the cogging torque of the machine is reduced due to the partial cancellation of the individual components. However, it is possible to further reduce the cogging torque without compromising machine performance by adjusting the magnet pole arc width. This technique is commonly used in the design of RF PM machines and is equally applicable to AF PM machines (Caricchi, 2004). Cogging torque is not particularly important in this application, but the exercise of designing the magnet pole arc so as to minimize the cogging torque is done regardless, as a "good" practice.

The 2-D transient simulation is run (as described in section 2.1) for magnet pole arcs (θ_m) varying between 65% and 90% of the pole-pitch (θ_p), with cogging torque outputs as shown in Fig. 4.11. The motion is set at a speed of approximately 1 pole-pitch per second in order to prevent bias in the results due to so-called "spinning losses" in the machine. Note that the expected 12 periods of cogging torque is indistinguishable in the waveforms shown due to the "noise" resulting from the FEA calculations. All of these plots show low cogging torque values, as is expected with NOW, but the important detail to notice is the initial trend of the torque waveforms. We can see that the waveform for $\theta_m = 0.65\theta_p$ is negative for the initial rotor position; but when the magnet pole arc to pole-pitch ratio is increased to 70%, the torque waveform becomes positive for the same initial rotor position. This means that there must be a magnet pole arc value between 65% and 70% of the pole-pitch that nulls the cogging torque. We see the same trend happen for magnet arcs between 80% and 85% of the pole-pitch. Since machine performance is better with the larger magnet pole arc, the latter range was investigated more closely. Fig. 4.12 indicates that the cogging torque is minimized for a magnet pole arc to pole-pitch ratio of approximately 0.81 and thus the magnets are designed to have $\theta_m = 13.25^o$.

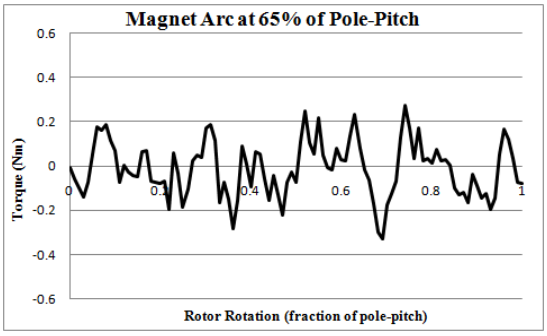

(a)

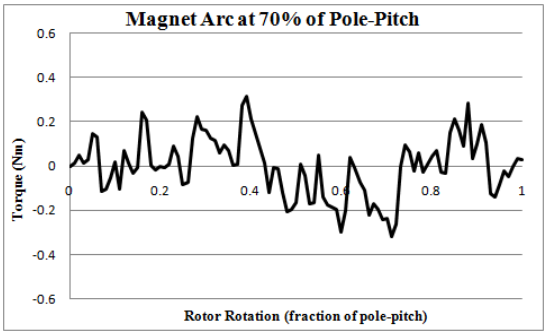

(b)

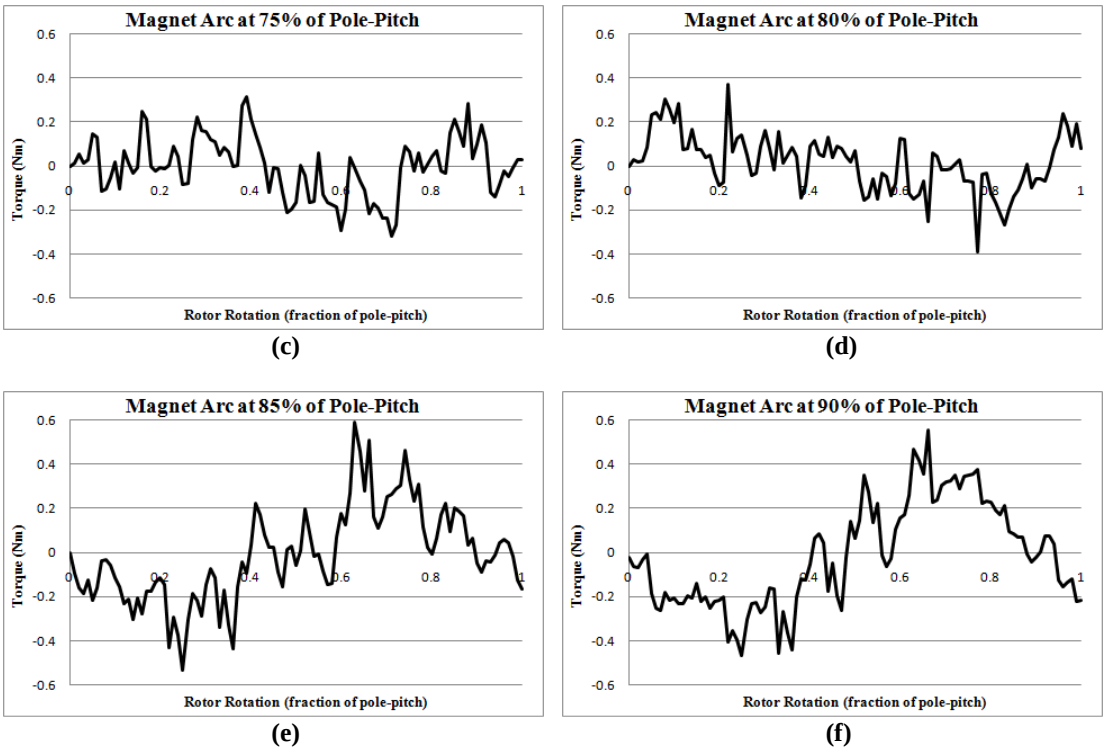

Fig. 4.11 Cogging torque waveforms for varying magnet pole arcs.

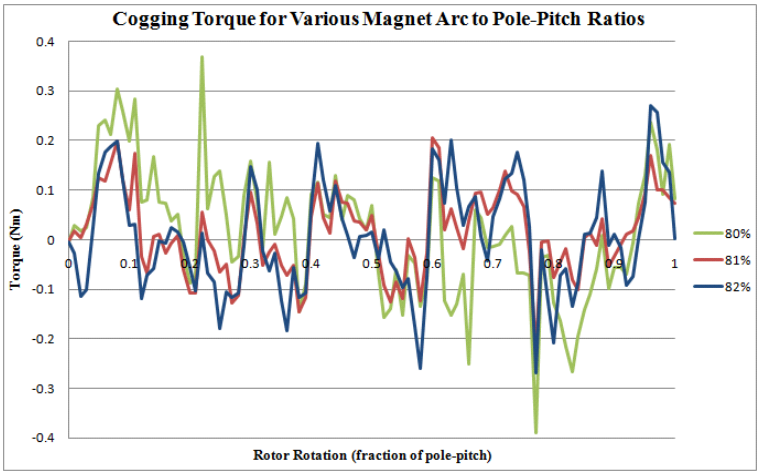

Fig. 4.12 Cogging torque waveforms for magnet pole arcs in the range of 80-82% of the pole pitch.

Chapter 5

Summary and Continuing Work

In this thesis, the design of an electric machine to perform as both a starter and alternator in a series hybrid electric vehicle has been detailed. The focus of the work is on practical design aspects specific to single-sided axial flux permanent magnet machines with non-overlapped windings. First, a characterization of the rotor losses in these machine types was presented through experimental validation of finite element analysis estimates. The approaches taken to model the axial flux geometry, especially in two-dimensions, were detailed, and the difficult issue of validating the finite element analysis estimates with experimental data was addressed with a prototype 24-slot, 20-pole single-sided machine fitted with single-layer non-overlapped windings. Next, the comparative advantages and disadvantages of the single-sided axial flux geometry were explored within the context of surface mount permanent magnet machines. New material was offered to highlight the benefits of the single-sided axial flux geometry and the constraints and assumptions made when making the comparisons were discussed in detail, including a study of the biases these can introduce. The basis of comparison was founded on constant electromagnetic airgap shear stress, being the product of electric and magnetic loading, and indeed the constancy of both those factors. The metrics used for comparison were the mass of the active materials and the volume essential to house said materials. A range of lesser issues that are relevant when choosing a machine structure were presented and discussed. Finally, the performance criteria for the integrated starter-alternator was quantified based on characterization of the internal

combustion engine and the energy storage system of the vehicle and a full account of the design process was detailed, including justification of all design choices.

The present laboratory facilities and available equipment at the author's institution allow electric machine and drive testing for only very low power machines (1 kW or less). However, a new laboratory space is currently being renovated and furnished with the intention of providing a platform for the testing of larger machines. Therefore it is possible for the work presented in this thesis to continue with future students. The purpose of this section is then to identify the up-to-date status of the project and outline the procedures and equipment necessary for completion of the prototype machine construction and testing.

Fabrication of the two aforementioned 7-kW prototype machines for the integrated starter-alternator has commenced. Fig. 5.1 shows the unassembled machines to illustrate the status of the process to date. Both stators have been formed by milling slots (as specified in Chapter 4) out of a tape-wound toroid of grade M12 silicon steel. Once the milling process was complete, the stators were soaked in a 50% phosphoric acid solution (H_3PO_4) in order improve isolation between the laminations that were shorted as a result of the machining. The stator coils have been formed by winding four strands of 16 AWG copper wire in-hand around an aluminum bobbin in the shape of a tooth and placed in the stator by hand for both the single- and double-layer configurations. The solder connections for the single-layer machine have been completed, but those of the double-layer machine are currently being made. The mechanical structure of the rotor assemblies has been finalized and the machining for said pieces is complete. All materials necessary for magnet installation have been acquired, though the magnet-gluing process has not yet begun. Finally, the frames that will house these two prototype machines have been designed and constructed.

In order to complete the fabrication, the following steps should be undertaken:

1. Finish making the solder connections for the double-layer machine.
2. Insert thermocouples into select windings on both stators so that the temperature of the coils can be monitored during testing.
3. Take the stators to be potted in resin and have mounting holes tapped through the yokes. Additionally, spaces for three Hall-effect sensors should be machined into the top of the stator teeth.
4. Glue the magnets onto the rotor plates and install the Hall-effect sensors.

5. Assemble the active components of the machines and mount to the frames.

It is estimated that this process would be completed in one month's time for a student working part-time if no significant issues are encountered.

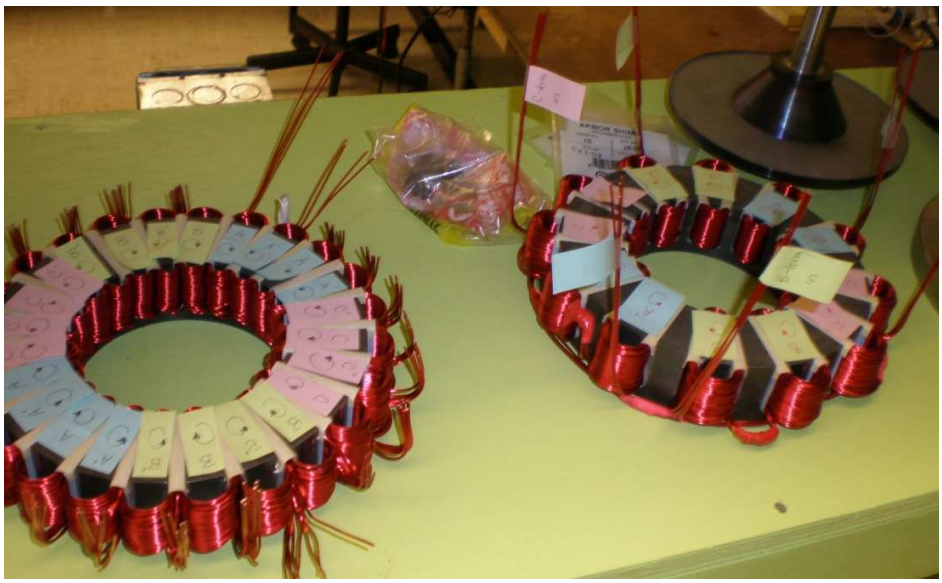

Fig. 5.1 Photographs of the machine assemblies to illustrate the fabrication process to-date. In (a) the rotor plates with shafts are shown along with the stator back-pieces with bearing insets, (b) shows the wound single- and double-layer stators and the motor mounting frames are shown in (c).

Before testing of the prototype machines can commence, some laboratory equipment should be purchased (or installed). First and foremost, a structurally sound and adjustable platform to affix the machines to during testing must be manufactured; ideally this would be fastened directly to the concrete floor of the lab. Secondly, dSPACE computing resources must be available and configured in order to interface with the DURApulse drive mentioned in Chapter 4. Finally, large power supplies should be acquired which have the capacity to provide the electrical power necessary to fully test these machines, even under overload conditions. It is worth noting that it is possible to test the machines at rated load by using a series connection of the two 3.3 kW (100 V, 33 A) power supplies that are currently available in the laboratory.

The intention of constructing two similar machines is that the machine under test can be run as a generator by connecting it through an in-line torque transducer to the other prototype machine which would be operating in motoring mode and interfaced to the drive electronics. With this configuration, the following tests should then be performed for each machine:

1. Machine constant confirmation. The purpose of this test is simply to verify that the machine constant is as designed for and that the winding connections have all been

made properly. The machine under test is run with no load connected and the open-circuit voltages (line-neutral) at the machine terminals are measured. It is not necessary to use a torque transducer between the two machines, but one can be placed there if required for coupling. A smooth, sinusoidal set of three-phase voltages should be seen and the machine constant in V/(rad/s) can be calculated using the magnitude and frequency information from the voltage waveform of a single phase.

2. Spinning loss measurement. In this, the machine under test is run with no load connected and a small capacity torque transducer should be used in order to obtain good precision. The 2D FEA estimation of rotor loss due to slotting is approximately 350 W at 3000 rpm (~1.2 Nm), so a torque transducer with a 2 Nm capacity would be ideal. Speed sensing should be done with either the Hall effect sensors in place or via an encoder. The mechanical input power to the generator can then be determined and since there is no load connected, the entirety of this power is the spinning loss encompassing power loss due to friction and windage, stator iron loss and rotor loss due to stator slotting. This test should be run for a full spectrum of speeds ranging up to rated speed.
3. Core loss measurement. This test should be performed on the extra, uncut stator toroid, as described in Chapter 2 for a range of frequencies from 60 to 500 Hz. A higher power amplifier may need to be acquired.
4. Spinning loss measurement where stator is replaced with an uncut toroid. Once the core loss measurement is completed, the uncut toroid should have mounting holes tapped into it to affix it to the machine frame containing the bearing. The "machine" assembly is then the same as if an actual stator was in place and the test setup is the same as previously described for spinning loss testing. The purpose of this measurement is to isolate the loss due to bearing friction. The airgap should be increased from 1 mm to 1.5 mm by adding shims (that have already been manufactured) between the bearing and the rotor brace such that the axial load in the bearing is equivalent to that of the actual machine. The mechanical power input to the "machine", which is entirely bearing loss, can then be measured.
5. Loaded tests up to rated load. A three-phase resistive load should be connected to the output of the generator. Two three-phase loads are currently available in the lab: one is fixed resistance (around 12 Ω) per phase rated at approximately 8 kW and the other is a 3.3 kW variable resistance load. These would suffice to test the machine at a few low power operating points and a single higher-power point; ideally another load would be acquired that is completely variable and rated at around 10 kW. Speed and torque

measurements should be taken as before, using the 20 Nm rated torque transducer, in order to calculate the mechanical power input to the generator. Voltage and current measurements on two of the phases should be used to calculate the electrical output of the generator. These measurements will be used to determine the generator efficiency at a range of operating points and also, in conjunction with the other aforementioned tests, to extract particular losses that are of interest.

6. Overload tests. The purpose here is to test the ability of the machine to supply the starting torque for the engine. It may not be possible to carry out these tests until a more established and larger-scale testing facility is made available, however, an overview of the process will still be given here. Firstly, a power supply and drive capable of handling the current (~ 100 Arms per phase) necessary for the machine to output 400% rated torque should be purchased and installed. Secondly a higher capacity torque transducer (rated at 80-100 Nm) should also be acquired. Finally, it is necessary to have a mechanical load to absorb the power (i.e. an eddy-current brake). In this setup, the machine under test is run in motoring mode, connected directly to the drive electronics at the input and to the mechanical load, through an in-line torque transducer, at the output. The ability of the machine to provide the necessary torque for a very short time period is assessed and the thermocouples placed in the stator windings are monitored.

In summary, this dissertation provided a full account of the design process for an integrated starter-alternator for a series hybrid vehicle. Justification of all design choices was provided through the investigation of several important aspects of electric machine design and the final result was a single-sided AF PM machine with a rating of 6.7 kW at 2800 rpm. The present laboratory facilities and available equipment at the author's institution allow electric machine and drive testing for only very low power machines (1 kW or less), so testing of a prototype machine was not possible. However, a new laboratory space is currently being renovated and furnished with the intention of providing a platform for the testing of larger machines. Therefore it is intended that the work presented in this thesis be continued with future students. To that aim, the current state of the prototype machine construction was identified the procedure for completion of construction was given. Additionally, the methods and equipment necessary for execution of the prototype machine testing was provided.

Bibliography

Alberti, L., Fornasiero, E., Bianchi, N., Bolognani, S., 2008. "Impact of Rotor Losses in a 12-Slot 10-Pole Axial Flux PM Machine", IEEE Industry Applications Conference, Oct. 2008, CD-ROM.

Aydin, M., Zhu, Z. Q., Lipo, T. A., Howe, D., 2007. "Minimization of Cogging Torque in Axial Flux Permanent Magnet Machines: Design Concepts", IEEE Transactions on Magnetics, Vol. 43, Issue 9, Sept. 2007, pp. 3614-3622.

Bianchi, N., Dai Pre, M., Grezzani, G., Bolognani, S., 2005. "Design Considerations on Fractional-Slot Fault-Tolerant Synchronous Motors", IEEE Transactions on Industry Applications, Vol. 42, Issue 4, July-Aug. 2006, pp. 997-1006.

Bianchi, N., Dai Pre, M., 2006. "Use of the Star of Slots in Designing Fractional-Slot Single-Layer Synchronous Motors", IEE Proceedings on Electric Power Applications, Vol. 153, Issue 3, Mar. 2006, pp. 459-466.

Bianchi, N., Dai Pre, M., Alberti, L., Fornasiero, E., 2007. "Theory and Design of Fractional-Slot PM Machines", IEEE Industry Applications Conference Tutorial Course Notes, Padova, Italy: CLEUP, 2007, ISBN 978-88-6129-122-5.

Bianchi, N., Bolognani, S., Dai Pre, M., 2008. "Magnetic Loading of Fractional-Slot Three-Phase PM Motors With Nonoverlapped Coils", IEEE Transactions on Industry Applications, Vol. 44, Issue 5, Sept.-Oct. 2008, pp. 1513-1521.

Bianchi, N., Bolognani, S., Fornasiero, E., 2010. "An Overview of Rotor Losses Determination in Three-Phase Fractional-Slot PM Machines", IEEE Transactions on Industry Applications, Vol. 46, Issue 4, Aug. 2010.

Caricchi, F., Crescimbini, F., Honorati, O., 1998. "Low-Cost Compact Permanent Magnet Machine for Adjustable-Speed Pump Application", IEEE Transactions on Industry Applications, Vol. 34, Issue 1, Jan.-Feb. 1998, pp. 109-116.

Caricchi, F., Capponi, F. G., Crescimbini, F., Solero, L., 2004. "Experimental Study on Reducing Cogging Torque and No-Load Power Loss in Axial-Flux Permanent Magnet Machines with Slotted Winding", IEEE Transactions on Industry Applications, Vol. 40, Issue 4, July-Aug. 2004, pp. 1066-1075.

Cavagnino, A., Lazzari, M., Profumo, F., Tenconi, A., 2002. "A Comparison Between the Axial Flux and Radial Flux Structures for PM Synchronous Motors", IEEE Transactions on Industry Applications, Vol. 38, Issue 6, Nov.-Dec. 2002, pp. 1517-1524.

Cros, J., Viarouge, P., 2002. "Synthesis of High Performance PM Motors With Concentrated Windings", IEEE Transactions on Energy Conversion, Vol.17, Issue 2, June 2002, pp. 248-253.

Dorrell, D., Popescu, M., Cossar, C., Ionel, D., 2008. “Unbalanced Magnetic Pull in Fractional-Slot Brushless PM Motors”, IEEE Industry Applications Conference, Oct. 2008, CD-ROM.

El-Refaie, A., Jahns, T., 2005. “Optimal Flux Weakening in Surface PM Machines Using Concentrated Windings”, IEEE Transactions on Industry Applications, May –June 2005, pp. 790-800.

El-Refaie, A., Jahns, T., Novotny, D. W., 2006. “Analysis of Surface Permanent Magnet Machines With Fractional-Slot Concentrated Windings”, IEEE Transactions on Energy Conversion, Vol. 21, Issue 1, Mar. 2006, pp. 34-43.

Han, S., Jahns, T., Zhu, Z., 2008. “Analysis of Rotor Core Eddy-Current Losses in Interior Permanent Magnet Synchronous Machines”, IEEE Transactions on Industry Applications, Vol. 46, Issue 1, Jan.-Feb. 2010, pp. 196-205.

Huang, S., Aydin, M., Lipo, T. A., 2001. “TORUS Concept Machines: Pre-Prototyping Design Assessment for Two Major Topologies”, IEEE Proceedings of the Industry Application Society Annual Meeting, Chicago, USA, 2001.

Huang, S., Jian, L., Leonardi, F., Lipo, T. A., 1999. “A Comparison of Power Density for Axial Flux Machines Based on General Purpose Sizing Equations”, IEEE Transactions on Energy Conversion, Vol. 14, No. 2, Jun. 1999.

Ishak, D., Zhu, Z., Howe, D., 2006. “Comparison of PM Brushless Motors, Having Either All Teeth or Alternate Teeth Wound”, IEEE Transactions on Energy Conversion, Vol. 21, No. 1, Mar. 2006, pp.95-103.

Jassal, A., Polinder, H., Shrestha, G., Versteegh, C., 2008. “Investigation of Slot Pole Combinations and Winding Arrangements for Minimizing Eddy Current Losses in Solid Back-Iron of Rotor for Radial Flux Permanent Magnet Machines”, Proceedings of the International Conference on Electric Machines, Sept. 2008, CD-ROM, Paper ID 1292.

Kamper, M., Rix, A., Wills, A., Gonzalez, A., 2008. “Formulation, Finite-Element Modeling and Winding Factors of Non-Overlap Winding Permanent Magnet Machines”, Proceedings of the International Conference on Electric Machines, Sept. 2008, CD-ROM, Paper ID 1170.

Kamper,M., Wang, R., Rossouw, F., 2008. “Analysis and Performance of Axial Flux Permanent-Magnet Machine With Air-Cored Nonoverlapping Concentrated Stator Windings”, IEEE Transactions on Industry Applications, Vol. 44, Issue 5, Sept.-Oct. 2008, pp. 1495-1504.

Kwon, T., Sul, S., Alberti, L., Bianchi, N., 2007. “Design and Control of an Axial-Flux Machine for a Wide Flux-Weakening Operation Region”, IEEE Industry Applications Conference, Sept. 2007, pp. 2175-2182.

Langford, C., Camilleri, S., 2010. “Axial flux electric machine”. US patent application 20100164313. Application filed July 1, 2010.

Magnussen, F., Sadarangani, C., 2003. “Winding Factors and Joule Losses of Permanent Magnet Machines With Concentrated Windings”, IEEE International Conference on Electric Machines and Drives, June 2003, pp. 333-339.

Magnussen, F., Lendenmann, H., 2007. “Parasitic Effects in PM Machines With Concentrated Windings”, IEEE Transactions on Industry Applications, Vol. 43, Issue 5, Sept.-Oct. 2007, pp. 1223-1232.

Marignetti, F., Tomassi, G., Cancelliere, P., Delli Colli, V., 2006. “Electromagnetic and Mechanical Design of a Fractional-Slot-Windings Axial-Flux PM Synchronous Machine with Soft Magnetic Compound Stator”, IEEE Industry Applications Conference, Vol. 1, Oct. 2006, pp. 62-69.

Miller, T. J. E., 1989. Brushless Permanent Magnet and Reluctance Motor Drives, Clarendon Press, Oxford, 1989.

Ombach, G., Junak, J., 2008. “Comparison of Double-Layer Interior Permanent Magnet Synchronous Motor Design With Two Different Pole Numbers”, Proceedings of the International Conference on Electrical Machines, Sept. 2008, CD-ROM, Paper ID 1014.

Nuscheler, R., 2008. “Two-Dimensional Analytical Model for Eddy-Current Loss Calculation in the Magnets and Solid Rotor Yokes of Permanent Magnet Synchronous Machines”, Proceedings of the International Conference on Electrical Machines, Sept. 2008, CD-ROM, Paper ID 1095.

Pang, Y., Zhu, Z. Q., Howe, D., 2006. “Analytical Determination of Optimal Split Ratio for Permanent Magnet Brushless Motors”, IEE Proceedings on Electric Power Applications, Vol. 153, No. 1, Jan. 2006, pp. 7-13.

Parviainen, A., Niemela, M., Pyrhonen, J., Mantere, J., 2005. “Performance Comparison Between Low-Speed Axial-Flux and Radial-Flux Permanent Magnet Machines Including Mechanical Constraints”, IEEE International Conference on Electric Machines and Drives, May 2005, pp. 1695-1702.

Patterson, D., Camilleri, S., Embery, L., 2010. “Automated manufacturing machine”. US patent 7654123. Feb. 2, 2010.

Polinder, H., Hoeijmakers, M., Scuotto, M., 2007. “Eddy-Current Losses in the Solid Back-Iron of PM Machines for Different Concentrated Fractional Pitch Windings”, IEEE International Conference on Electric Machines and Drives, Vol. 1, May 2007, pp 652-657.

Ragot, P., Germano, P., Markovic, M., Perriard, Y., 2008. “Brushless DC Motor for a Solar Airplane Application: Comparison Between Simulations and Measurements”, IEEE Industry Applications Conference, Oct. 2008, CD-ROM.

Rahman, Z., 2004. “Evaluating Radial, Axial and Transverse Flux Topologies for ‘In-Wheel’ Motors”, IEEE Power Electronics in Transportation, 2004, pp. 75-81.

Saban, D., Lipo, T., 2007. “Hybrid Approach for Determining Eddy-Current Losses in High-Speed PM Rotors”, IEEE International Electric Machines and Drives Conference, Vol. 1, May 2007, pp. 658-661.

Salminen, P., 2004. “Fractional Slot Permanent Magnet Synchronous Motor for Low Speed Applications”, Dissertation, Lappeenranta University of Technology, Lappeenranta, Finland. ISBN 951-764-982-5.

Simsir, N. B., Ertan, H. B., 1999. “A Comparison of Torque Capabilities of Axial Flux and Radial Flux Type of Brushless DC (BLDC) Drives for Wide Speed Range Applications”, IEEE International Conference on Power Electronics and Drive Systems, Hong Kong, July 1999.

Sitapati, K., Krishnan, R., 2001. “Performance Comparisons of Radial and Axial Field Permanent-Magnet, Brushless Machines”, IEEE Transactions on Industry Applications, Vol. 37, Issue 5, Sept.-Oct. 2001, pp. 1219-1226.

Soinski, M., 1984. “Application of the Anisometric Method for Determining Polar Curves of Induction, Apparent Core Loss and Core Loss in Cold-Rolled Electrical Sheets of Goss Texture”, IEEE Transactions on Magnetics, Vol. 20, Issue 1, Jan. 1984, pp. 172-183.

Spooner, E., Chalmers, B. J., 1992. “TORUS: A Slotless, Toroidal-Stator, Permanent Magnet Generator”, IEE Proceedings B Electric Power Applications, Vol. 139, Issue 6, Nov. 1992, pp. 497-506.

Ugalde, G., Poza, J., Rodriguez, M., Gonzalez, A., 2008. “Space Harmonic Modeling of Fractional Permanent Magnet Machines From Star of Slots”, Proceedings of the International Conference on Electrical Machines, Sept. 2008, CD-ROM, Paper ID 1052.

Wang, J., Xia, Z. P., Long, S. A., Howe, D., 2006. “Radial Force Density and Vibration Characteristics of Modular Permanent Magnet Brushless AC Machine”, IEE Proceedings on Electric Power Applications, Vol. 153, Issue 6, Nov. 2006, pp. 793-801.

Wrobel, R., Mellor, P., 2008. “Design Considerations of a Direct Drive Brushless Machine With Concentrated Windings”, IEEE Transactions on Energy Conversion, Vol. 23, Issue 1, Mar. 2008, CD-ROM.

Yamazaki, K., Fukushima, Y., Sato, M., 2008. “Loss Analysis of Permanent Magnet Motors With Concentrated Windings – Variation of Magnet Eddy Current Loss Due to Stator and Rotor Shapes”, IEEE Industrial Applications Conference, Oct. 2008, CD-ROM.

Zhang, Z., Profumo, F., Tenconi, A., 1996. “Axial-Flux Versus Radial-Flux Permanent-Magnet Motors”, Electromotion, Vol. 3, 1996, pp. 134-140.

Zhu, Z., Howe, D., Bolte, E., Ackermann, B., 1993. “Instantaneous Magnetic Field Distribution in Brushless Permanent Magnet DC Motors, Part I: Open-Circuit Field”, IEEE Transactions on Magnetics, Vol. 29, No. 1, Jan. 1993, pp. 124-135.

Zhu, Z., Howe, D., 1993. “Instantaneous Magnetic Field Distribution in Brushless Permanent Magnet DC Motors, Part II: Armature-Reaction Field”, IEEE Transactions on Magnetics, Vol. 29, No. 1, Jan. 1993, pp. 136-142.

Zhu, Z., Howe, D., 1993. “Instantaneous Magnetic Field Distribution in Brushless Permanent Magnet DC Motors, Part III: Effect of Stator Slotting”, IEEE Transactions on Magnetics, Vol. 29, No. 1, Jan. 1993, pp. 143-151.

Zhu, Z., Howe, D., 1993. “Instantaneous Magnetic Field Distribution in Brushless Permanent Magnet DC Motors, Part IV: Magnetic Field on Load”, IEEE Transactions on Magnetics, Vol. 29, No. 1, Jan. 1993, pp. 152-158.

Appendix A: Split Ratio Calculations for Axial Flux Machines

The purpose of this appendix is to provide the details of the calculations regarding specific torque and torque density of AF machines as functions of split ratio, the results of which are provided in section 4.2. The parameters listed in Table 4.1 are all assumed to be predetermined quantities used to perform the geometrical calculations identified here.

A.1 Specific Torque and Monetary Cost

The specific torque of an AF PM machine is defined as the torque per unit mass of the active materials. To determine this quantity, the total volumes of magnet material, steel and copper must each be defined in terms of geometrical parameters and design criteria.

The volume of magnet material necessary in each design can be calculated as in (A.1) where l_m, the axial thickness of the magnets, is determined from (A.2).

$$V_{mag} = \pi\left(r_o^2 - r_i^2\right)\frac{\theta_m}{\theta_p} l_m \tag{A.1}$$

$$B_m = B_r \frac{l_m}{l_m + l_g} \tag{A.2}$$

The volume of steel in the rotor backiron, $V_{s,r}$ is given by (A.3) where the rotor thickness, l_r, is designed to exactly match that required for electromagnetic purposes as discussed in Chapter 3 and given by the expression in (A.4). The number of poles (p) in the machine is calculated from the predefined number of poles per meter length at the average machine radius (P) as in (A.5).

$$V_{s,r} = \pi r_o^2 l_r \tag{A.3}$$

$$l_r = \frac{\pi r_{av}}{p}\frac{\theta_m}{\theta_p}\frac{B_m}{B_t} \tag{A.4}$$

$$p = 2\pi r_{av} P \tag{A.5}$$

The stator geometry is slightly more challenging to define as the total volume of steel in the stator, $V_{s,s}$, is dependent upon the slot geometry as shown in (A.6). We begin the derivation of the expression for circumferential slot width (w_s) by first defining the magnetic loading (B_m) and maximum steel flux density (B_t) in terms of the flux per pole (ϕ_{pole}) and geometrical quantities as shown in (A.7) and (A.8). Solving each of these for ϕ_{pole}, equating them and rearranging, yields the expression for slot width shown in (A.9). The number of slots in the machine (N_s) is calculated from the predefined number of slots per meter length at the average machine radius (Q) as in (A.10). A discussion regarding determination of the axial slot length (l_s) from fundamental design criteria is given in Chapter 3, although the equation is provided here in (A.11) for completeness.

$$V_{s,s} = \left(l_y + l_s\right)\pi\left(r_o^2 - r_i^2\right) - l_s w_s (r_o - r_i) N_s \tag{A.6}$$

$$B_m = \frac{\varphi_{pole}}{\left(\frac{\theta_m}{\theta_p}\right)\left(\frac{2\pi r_{av}}{p}\right)(r_o - r_i)} \tag{A.7}$$

$$B_t = \frac{\varphi_{pole}}{\left(\frac{2\pi r_{av}}{N_s} - w_s\right)(r_o - r_i)\left(\frac{N_s}{p}\right)} \tag{A.8}$$

$$w_s = \left(1 - \frac{\theta_m}{\theta_p}\frac{B_m}{B_t}\right)\frac{\pi(r_o + r_i)}{N_s} \tag{A.9}$$

$$N_s = 2\pi r_{av} Q \tag{A.10}$$

$$l_s = \frac{A_e}{J}\left[\frac{B_t}{B_t - \frac{\theta_m}{\theta_p} B_m}\right] \tag{A.11}$$

The necessary stator yoke thickness, l_y, is based on the same principles governing the rotor backiron design and is defined in (A.12). The total steel volume in the machine is then the sum of the rotor steel ($V_{s,r}$) and stator steel ($V_{s,s}$).

$$l_y = \frac{\pi r_{av}}{N_s}\frac{\theta_m}{\theta_p}\frac{B_m}{B_t} \tag{A.12}$$

The calculations regarding the amount of copper in an AF PM machine are inclusive of details regarding the specific winding scheme utilized as it impacts the arrangement of the end-turns of the windings. It is assumed that NOW are used and calculations for both SL and DL layouts are presented here, although in practice, there are only particular slot-pole combinations that lend themselves to a SL winding (Bianchi, 2007). The geometry of the coils in an AF machine is shown in Fig. A.1 for both cases. It is apparent that there is less copper in each end-turn with a DL winding; however, there are twice as many coils as are present in the SL case. The curvature of the machine is neglected in the ensuing calculations and it is assumed that all of the end-turns, at both the inner and outer radii of the machine, have a semicircular surface area (Fig. A.1).

The added radial length of the machine due to the end turns in both the inward ($l_{e,i}$) and outward ($l_{e,o}$) directions can be determined by (A.13) for SL and (A.14) for DL, where the tooth with, w_t, is calculated at the inner ($w_{t,i}$) or outer ($w_{t,o}$) radius, respectively as in (A.15) and (A.16).

$$l_e = w_s + \frac{w_t}{2} \tag{A.13}$$

$$l_e = \frac{w_s + w_t}{2} \tag{A.14}$$

$$w_{t,i} = \frac{2\pi r_i - N_s w_s}{N_s} \tag{A.15}$$

$$w_{t,o} = \frac{2\pi r_o - N_s w_s}{N_s} \tag{A.16}$$

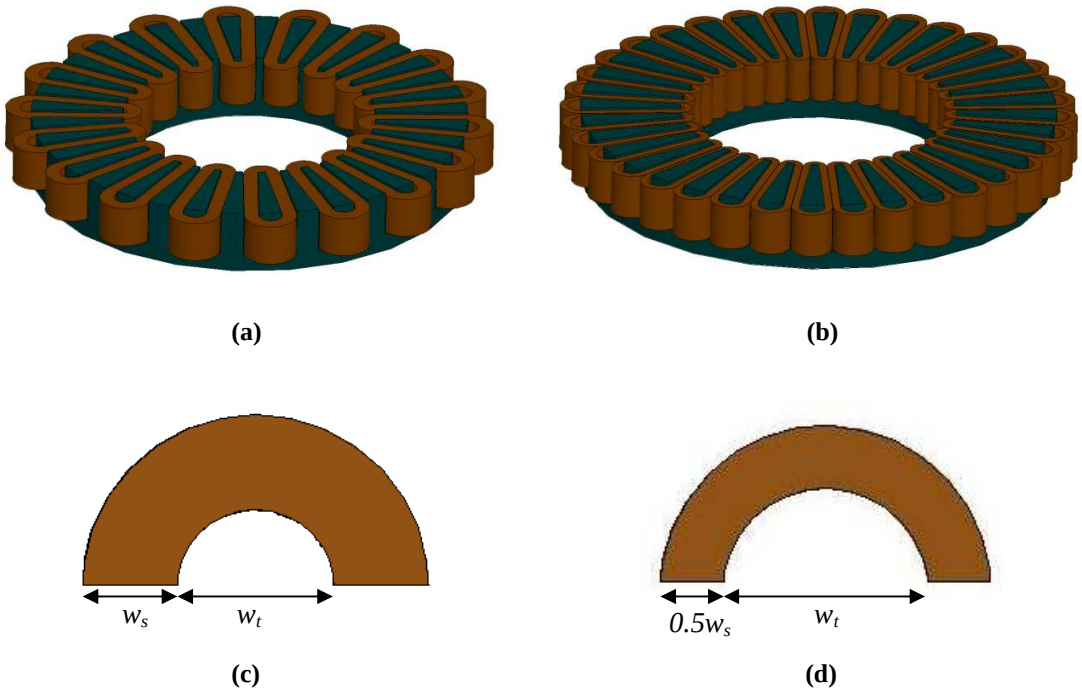

Fig. A.1. An AF stator is shown with SL and DL NOW in (a) and (b) respectively, while (c) and (d) show the geometry of the end-windings for the SL and DL cases.

The volume of copper that is contained in the slots of the machine ($V_{Cu,s}$) is as shown in (A.17) regardless of the winding type, where *ff* indicates the slot fill factor. The volume of copper wasted in the end-turns ($V_{Cu,e}$) is given by (A.18) for a SL winding and (A.19) for a DL winding. Note that the terms $l_{e,o}$ and $l_{e,i}$ in these two equations should be calculated appropriately for the winding type under consideration. The total volume of copper is then the sum of $V_{Cu,s}$ and $V_{Cu,e}$.

$$V_{Cu,s} = w_s l_s ff (r_o - r_i) N_s \tag{A.17}$$

$$V_{Cu.e}\left[\frac{\pi\left(l_{e,o}^2 - {w_{t,o}^2}/{4}\right)}{2} + \frac{\pi\left(l_{e,i}^2 - {w_{t,i}^2}/{4}\right)}{2}\right]\left(\frac{N_s}{2}\right) l_s ff \tag{A.18}$$

$$V_{Cu.e}\left[\frac{\pi\left(l_{e,o}^2 - {w_{t,o}^2}/{4}\right)}{2} + \frac{\pi\left(l_{e,i}^2 - {w_{t,i}^2}/{4}\right)}{2}\right] N_s l_s ff \tag{A.19}$$

The total mass of active material in the machine (m_{tot}) is then determined by summing the total volumes of magnet material, steel and copper multiplied by the respective densities (ρ_{NdFeB} = 7400 kg/m^3, ρ_{steel} = 7800 kg/m^3 and ρ_{Cu} = 8900 kg/m^3). The specific torque is calculated by dividing the torque output of the specific machine design by the mass of active material.

In order to calculate the monetary cost of each design, the individual masses of magnet material, steel and copper are multiplied by an estimated cost per mass ($/kg). The specific values used for the trend shown in Fig. 4.5 are $38/kg for NdFeB, $1.50/kg for the steel and $4.40/kg for copper (as of mid-year in 2009).

A.2 Torque Density

The concept of torque density differs slightly from that of specific torque not only in the units of measure, but also in that specific torque takes into account only the active materials of the machine while the complete package size is considered when defining the torque density. The total volume of the machine (V_{pack}) is regarded as a cylinder where the diameter includes the winding end-turns and the height is the total axial length of the machine as given in (A.20). Again, the term $l_{e,o}$ should be calculated according to whether the machine is fitted with SL or DL windings. The torque density is calculated by dividing the torque output of the specific machine design by the total package volume.

$$V_{pack} = \pi\left(r_o + l_{e,o}\right)^2\left(l_y + l_s + l_g + l_m + l_r\right) \tag{A.20}$$

A.3 Featured Geometries

Table A.1 details the specific geometries considered for the discussion presented in section 4.2 along with results of the calculations described in this appendix, where the parameters listed in Table 4.1 have the values indicated there and the assumptions listed in section 4.3 hold true. The

aforementioned assumptions fix several calculations to be constant across all the designs: w_s = 10.4167 mm, l_s = 15.0 mm, l_y = 3.125 mm, l_r = 4.6875 mm and l_m = 4.0 mm.

TABLE A.1 Calculation Results for Machine Designs Featured in Section 4.3

r_o (mm)	r_i (mm)	α_{SR}	τ (Nm)	N_s	$w_{t,o}$ (mm)	$w_{t,i}$ (mm)	$l_{e,o}$ (mm)	$l_{e,i}$ (mm)	p	V_{cu} (mm^3)	V_{st} (mm^3)	V_{mag} (mm^3)	M_{tot} (kg)	V_{pack} (m^3)	*Cost* ($)
190	183	0.963	22.95	70.31	6.563	5.937	8.490	8.177	46.87	109852	603390	24608	5.866	.00344	18.28
191	184	0.963	22.94	70.69	6.561	5.934	8.489	8.178	47.12	110441	609386	24740	5.919	.00348	18.41
178	170	0.955	22.86	65.60	6.633	5.867	8.525	8.142	43.73	106589	543115	26239	5.379	.00304	17.91
179	171	0.955	23.17	65.97	6.631	5.869	8.524	8.143	43.98	107202	548812	26389	5.430	.00307	18.04
169	160	0.947	22.80	62.02	6.706	5.794	8.561	8.105	41.34	104645	501990	27907	5.053	.00275	17.82
161	151	0.938	23.13	58.81	6.784	5.716	8.600	8.066	39.21	102914	467484	29405	4.780	.00251	17.77
154	143	0.929	22.83	55.98	6.867	5.633	8.642	8.025	37.32	101465	439053	30791	4.556	.00231	17.77
155	144	0.939	23.16	56.36	6.863	5.637	8.634	8.027	37.57	102148	444208	30998	4.603	.00234	17.91
148	136	0.919	22.99	53.53	6.954	5.546	8.685	7.981	35.69	100370	416245	32120	4.378	.00215	17.83
149	137	0.919	22.98	53.91	6.949	5.551	8.683	7.984	35.94	101076	421279	32346	4.425	.00217	17.98
144	131	0.910	23.19	51.84	7.038	5.462	8.727	7.939	34.56	100429	403636	33694	4.292	.00204	18.13
143	130	0.909	22.81	51.46	7.044	5.456	8.730	7.937	34.31	99698	398695	33449	4.245	.00201	17.97
139	125	0.899	22.88	49.76	7.134	5.366	8.775	7.891	33.18	99522	386124	34834	4.155	.00191	18.21
135	120	0.889	22.83	48.07	7.230	5.270	8.824	7.843	32.04	99133	373530	36050	4.063	.00181	18.39
132	116	0.879	22.81	46.75	7.325	5.175	8.871	7.796	31.17	99333	365666	37398	4.013	.00173	18.68
131	115	0.878	23.07	46.37	7.334	5.166	8.875	7.791	30.91	98532	360913	37096	3.967	.00171	18.51
128	111	0.867	22.87	45.05	7.435	5.065	8.923	7.741	30.03	98544	352962	38293	3.914	.00164	18.76
125	107	0.856	22.86	43.73	7.543	4.957	8.980	7.687	29.15	98391	344891	39358	3.857	.00157	18.96
123	104	0.846	23.07	42.79	7.645	4.855	9.031	7.636	28.53	98945	341353	40649	3.844	.00152	19.30
120	100	0.833	22.86	41.47	7.765	4.735	9.091	7.576	27.65	98486	333009	41469	3.781	.00146	19.41

r_o (mm)	r_i (mm)	α_{SR}	τ (Nm)	N_s	$w_{t,o}$ (mm)	$w_{t,i}$ (mm)	$l_{e,o}$ (mm)	$l_{e,i}$ (mm)	p	V_{cu} (mm^3)	V_{st} (mm^3)	V_{mag} (mm^3)	M_{tot} (kg)	V_{pack} (m^3)	Cost ($)
118	97	0.822	23.06	40.53	7.878	4.622	9.147	7.519	27.02	98780	329160	42553	3.761	.00141	19.69
116	94	0.810	22.81	39.58	7.996	4.504	9.206	7.460	26.39	98957	325155	43542	3.739	.00137	19.92
113	89	0.788	22.83	38.08	8.230	4.270	9.323	7.343	25.38	99947	321305	45691	3.734	.00131	20.52
111	86	0.775	22.86	37.13	8.365	4.135	9.391	7.276	24.76	99794	316825	46417	3.703	.00127	20.67
110	84	0.764	23.06	36.57	8.484	4.016	9.450	7.216	24.38	100559	316841	47539	3.718	.00125	21.01
107	79	0.738	22.82	35.06	8.759	3.741	9.588	7.079	23.37	100795	311763	49084	3.692	.00119	21.40
106	77	0.726	22.88	34.49	8.891	3.609	9.654	7.013	23.00	101325	311348	50017	3.700	.00117	21.68
105	75	0.714	22.90	33.93	9.028	3.472	9.722	6.944	22.62	101785	310797	50894	3.707	.00115	21.93
104	73	0.702	22.88	33.36	9.169	3.331	9.793	6.874	22.24	102174	310111	51714	3.711	.00113	22.17
103	71	0.689	22.83	32.80	9.312	3.185	9.866	6.801	21.87	102492	309289	52477	3.713	.00111	22.39
102	68	0.667	23.15	32.04	9.583	2.917	10.00	6.667	21.36	104141	312098	54475	3.764	.00110	23.05
101	66	0.653	23.00	31.48	9.743	2.757	10.08	6.587	20.99	104271	310895	55088	3.761	.00108	23.21
100	64	0.640	22.81	30.91	9.909	2.591	10.16	6.504	20.61	104330	309557	55644	3.755	.00106	23.35
100	63	0.630	23.16	30.72	10.03	2.437	10.22	6.442	20.48	105614	313048	56841	3.802	.00106	23.78
99	61	0.616	22.92	60.16	10.21	2.292	10.31	6.354	20.11	105555	311464	57303	3.793	.00104	23.89
98	58	0.592	22.94	29.41	10.52	1.976	10.47	6.197	19.60	106592	312962	58811	3.825	.00103	24.37
97	55	0.567	22.86	28.65	10.86	1.645	10.64	6.031	19.10	107440	314048	60168	3.851	.00101	24.80
97	54	0.557	23.10	28.46	11.00	1.504	10.71	5.960	18.98	108512	317045	61195	3.892	.00101	25.17
96	51	0.531	22.91	27.71	11.35	1.148	10.88	5.782	18.47	109101	317556	62345	3.909	.00100	25.52
96	50	0.521	23.10	27.52	11.50	0.999	10.96	5.708	18.35	110079	320332	63297	3.947	.00100	25.86
95	47	0.495	22.80	26.77	11.88	0.616	11.15	5.516	17.84	110409	320269	64239	3.956	.00098	26.13
95	46	0.484	22.95	26.58	12.04	0.458	11.23	5.437	17.72	111293	322825	65116	3.990	.00099	26.45

Appendix B: Background Theory for Non-Overlapped Windings

The purpose of this appendix is to provide a brief introduction to the differences between traditional, full-pitched windings and the recently developed non-overlapped winding (NOW) schemes, primarily in terms of the harmonic content in the MMF waveforms (winding function waveforms). In (2007), Bianchi et al. prepared a comprehensive resource detailing the design of NOW machines, so the brief treatment here is only information pertinent to the understanding of the material in this dissertation. The benefits of NOW are touted in the introduction, but the drawback of these windings is that the carefully developed sinusoidal MMF waveform in a full-pitched winding is transformed into more of a square wave with NOW. The impacts of this will be discussed here. Additionally, there are some slot-pole combinations that can be designed with a single-layer (SL) NOW, in which a winding is placed around every other tooth, as opposed to a double-layer (DL) scheme, where there is a coil around every tooth, and the differences in the MMF waveforms with these two layouts will also be explained.

The winding functions for a single phase of both the 24-slot/20-pole and the 24-slot/22-pole machines discussed in this paper for both the SL and DL cases are shown in Fig. B.1. Note that the total number of turns per phase is equivalent in both the DL and SL cases; that is, the SL scheme has half the number of coils as the DL case, but each winding has twice as many turns.

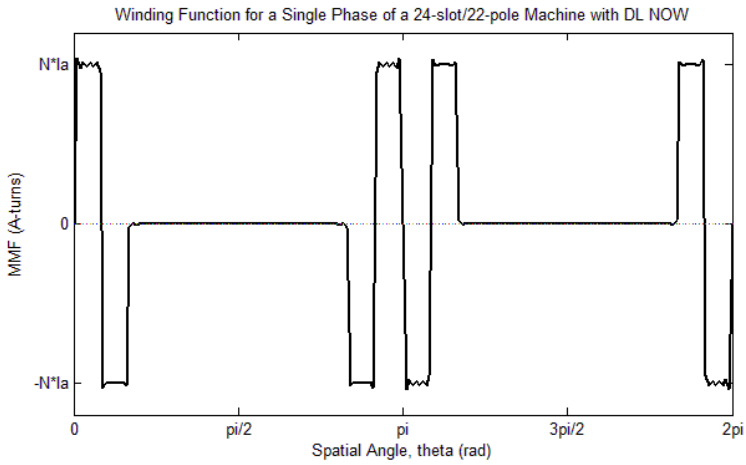

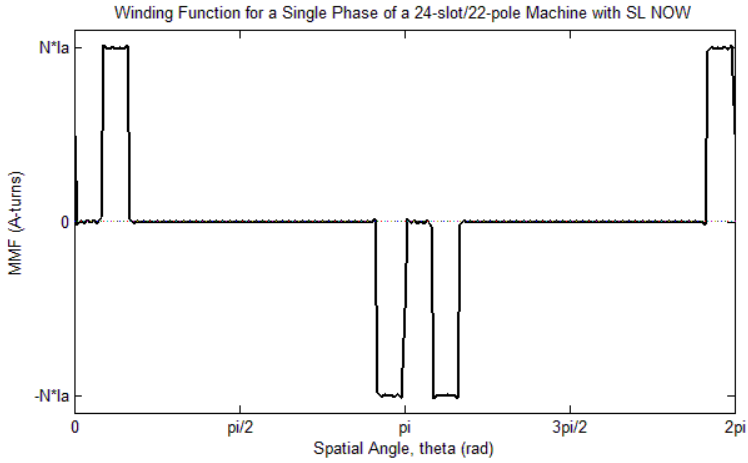

(a)

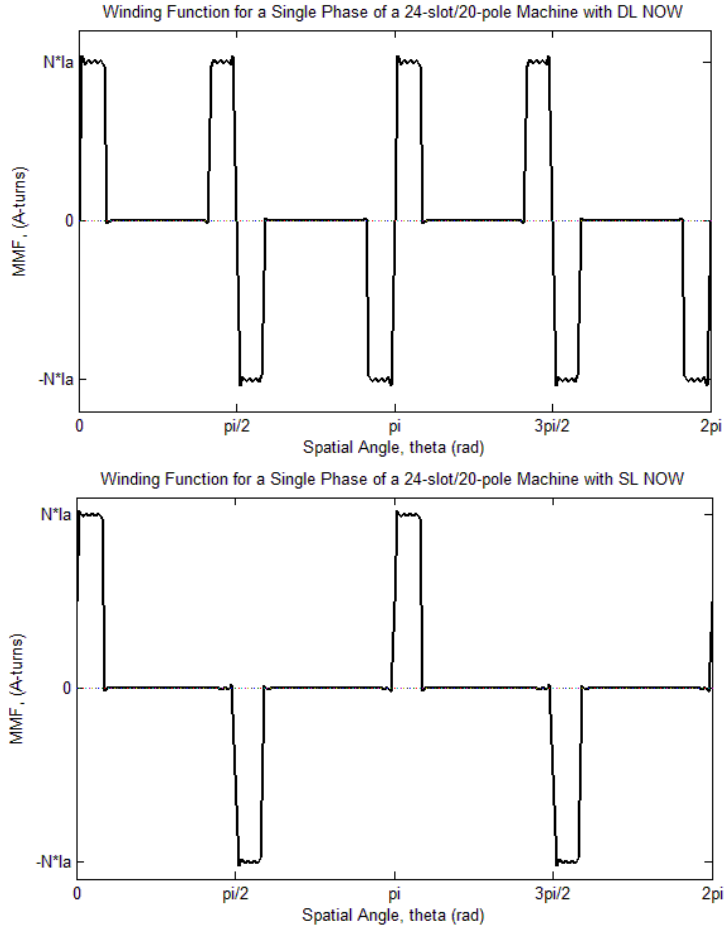

(b)

Fig. B.1. Winding functions for a single phase of (a) a 24-slot/22-pole machine and (b) a 24-slot/20-pole machine with both SL and DL NOW.

The complete winding functions for these two machines (both SL and DL cases) are shown in Fig. B.2 for an arbitrary time instant. From this figure, it is obvious that the MMF waveform resulting from current flow in the windings is far from sinusoidal and contains many harmonic components. The main, torque producing harmonic ($\upsilon = p/2$) is included in these plots for comparison.

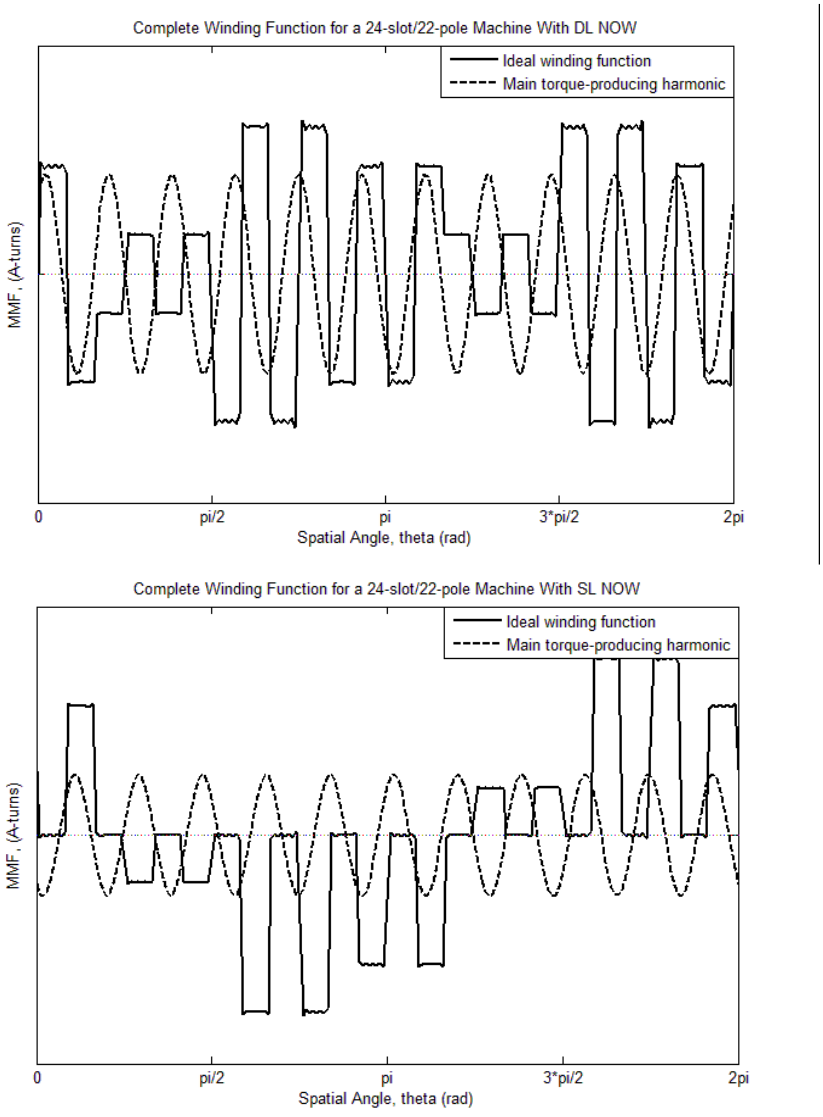

(a)

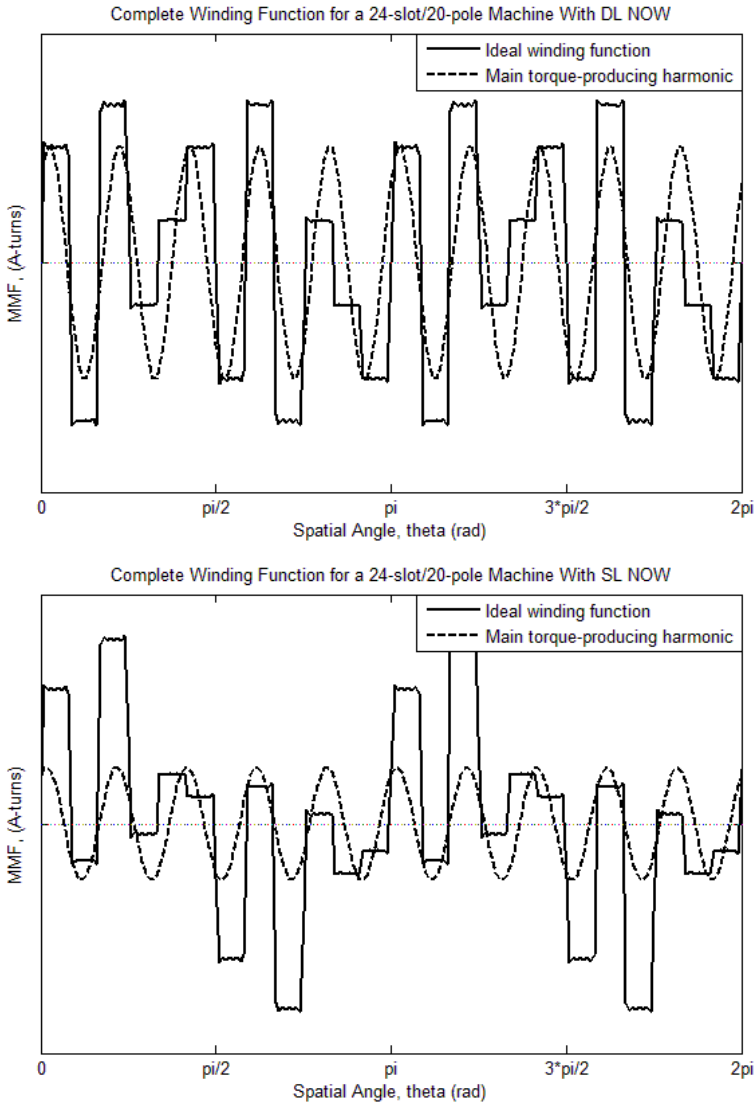

(b)

Fig. B.2. Complete winding functions for (a) a 24-slot/22-pole machine and (b) a 24-slot/20-pole machine with both SL and DL NOW shown at an arbitrary time instant.

Fourier series expansions, on a 2π-period, of the single-phase winding functions are shown in Fig. B.3 to illustrate the harmonic spectrum present. The two primary impacts of these harmonics are that (1) the winding factor of the main harmonic is reduced in comparison to the full-pitched winding case and (2) the rotor losses of the machine are increased. The latter effect is due to the fact that the rotor motion locks to that of the main harmonic so that the remaining harmonics rotate asynchronously with the rotor and cause a time-varying flux waveform in the rotor

components; obviously these time-varying flux waveforms cause eddy-current losses in the rotor. Of specific concern are the subharmonics (the spatial harmonics with number less than the main harmonic) because these penetrate more deeply into the rotor and cause higher losses. It is seen in Fig. B.3 that the SL windings have subharmonics with higher magnitudes than those of the DL windings, so the rotor losses are higher with the SL cases (Bianchi, 2010).

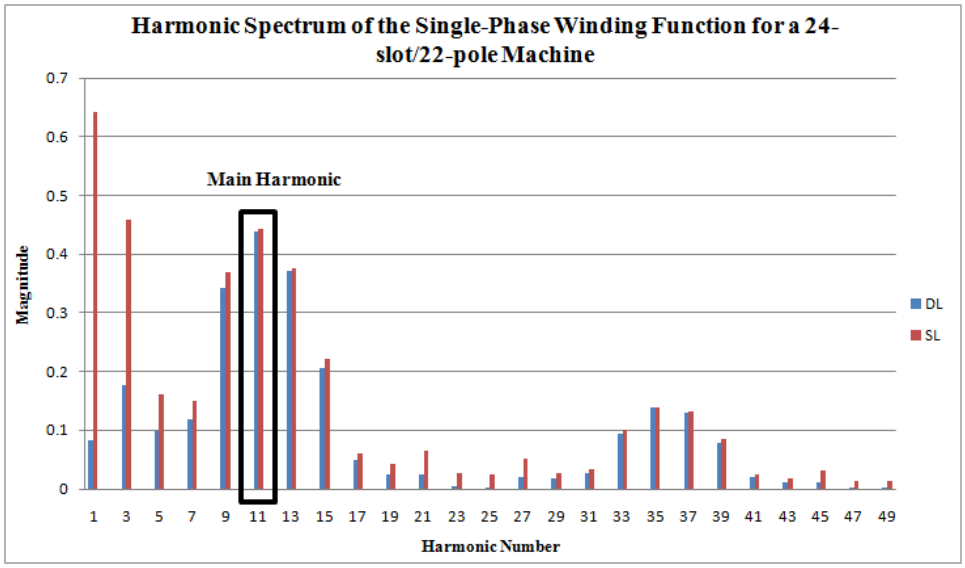

(a)

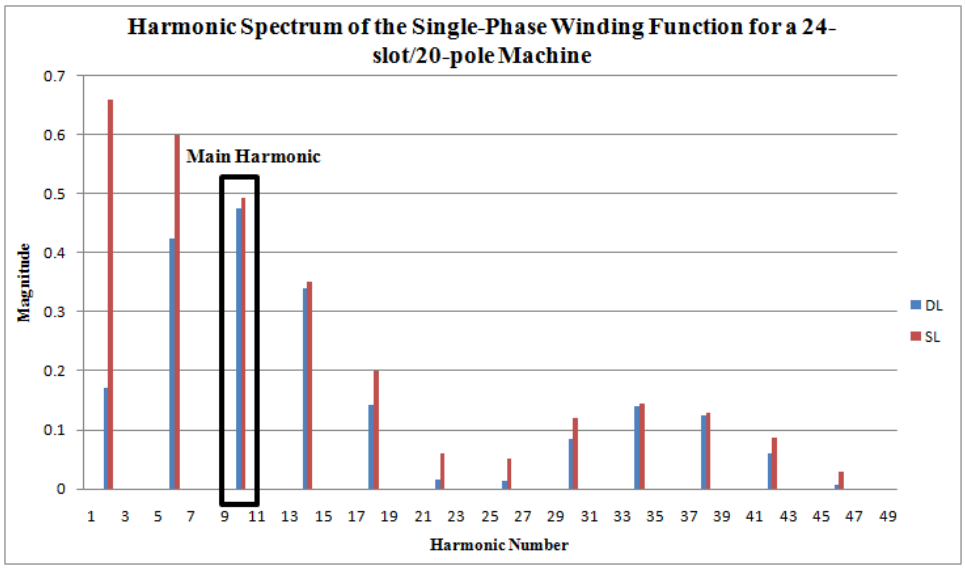

(b)

Fig. B.3. Fourier series expansions, on a 2π-period, of the single-phase winding functions for (a) a 24-slot/22-pole machine and (b) a 24-slot/20-pole machine.